Faculty 13
Institute for Theoretical Physics
Goethe University Frankfurt am Main

Dark Matter Effects on the Black Hole Shadows of Sgr A* and M87*

A thesis submitted for the degree of Master of Science in Physics

by

Lukas Prinz, born on August 23, 1997 in Gelnhausen
Matriculation number: 6333140

First supervisor: Prof. Dr. Laura Sagunski
Second supervisor: Dr. Alejandro Cruz-Osorio

November 29, 2022

Contents

Conventions, notation and abbreviations **4**

1 Introduction **5**
1.1 Dark matter . . . 5
1.2 Black holes and black hole shadows . . . 7
1.3 Black hole shadows as a probe of dark matter . . . 8
1.4 Structure of this thesis . . . 10

2 Theoretical preliminaries **11**
2.1 Dark matter models . . . 11
2.1.1 Cold collisionless dark matter . . . 11
2.1.2 Self-interacting dark matter . . . 11
2.1.3 Dark matter density spikes . . . 12
2.2 Technical description of black holes . . . 13
2.3 Geodesic motion . . . 15
2.4 Circular orbits around a Kerr black hole . . . 17

3 Method **19**
3.1 Modeling the dark matter halos . . . 19
3.2 Deriving a metric of a spacetime of a black hole in a dark matter halo . . . 21
3.2.1 Geometry of a dark matter halo . . . 21
3.2.2 Including a Schwarzschild black hole . . . 23
3.2.3 Introducing a spin parameter . . . 25
3.2.4 Restricting the dark matter halo's size . . . 25
3.3 Equations of motion for photons . . . 26
3.4 Technical definition of a black hole shadow and Bardeen's coordinates . . . 28
3.5 Performing the black hole shadow calculations . . . 32

4 Results **34**
4.1 Densities of the dark matter halos . . . 34
4.2 Properties of the black hole shadows . . . 37
4.3 Semi-analytical results on the width of a black hole shadow . . . 47
4.4 Uncertainty and measurability estimates . . . 49
4.5 Limitations . . . 53

5 Summary and outlook **54**

References **56**

A Appendix **62**
A.1 Existence of an outermost event horizon 62
A.2 Solutions to equation (4.2) 62

B Acknowledgments **64**

C Declaration of originality **65**

Conventions, notation and abbreviations

In this thesis, the Einstein summation convention will be used: If an index appears twice in an equation, a summation over that index over its entire range, usually $0, ..., 3$, is implied unless stated otherwise. We will choose the sign convention $(-+++)$ for the signature of the Lorentzian metric underlying relativistic spacetime.
Also take note of the following two tables for abbreviations and symbols in mathematical expressions that might need clarification.

Abbreviation	Meaning
GR	General Relativity
DM	Dark matter
CDM	Cold collisionless dark matter
SIDM	Self-interacting dark matter
BH	Black hole
SMBH	Supermassive black hole
MW	Milky Way
M87	Messier 87
Sgr A*	Sagittarius A*
EHT	Event Horizon Telescope
NFW	Navarro-Frenk-White

Symbol	Meaning
$\mathbb{R}^+$ / $\mathbb{R}_0^+$	The set of all positive / non-negative real numbers
$\dot{f}$, f'	The derivative of a function f of a single variable
$\partial_\mu f$	The partial derivative of a function f of several variables with respect to the μ-th variable
$r \to 0^+$	r approaches 0 from above
$f \circ g$	Composition of two functions f and g
G	Newton's gravitational constant
c	The speed of light in vacuum
$M_\odot$	The solar mass
pc	Parsec
as	Arcsecond

1 Introduction

1.1 Dark matter

The theory of General Relativity (GR) as the theory of gravity and the Standard Model of particle physics are very successful in explaining a wide range of physical phenomena, yet there are large discrepancies between the predictions of these established theories and, among others, observations on galactic and cosmological scales.
Though not historically the first, one easily accessible example to demonstrate this is the study of rotation curves of galaxies. Imagine an axisymmetric galaxy containing a star of mass $m \in \mathbb{R}^+$ which is subject to only gravity on a circular orbit of some radius $r \in \mathbb{R}^+$ around the galaxy's center. The star has a certain rotation velocity $v \in \mathbb{R}_0^+$ which generally depends on r. A plot of the correspondence $r \mapsto v(r)$ is called the galaxy's rotation curve and its shape mainly depends on how gravitating matter is distributed in the galaxy. A very simple calculation within the Newtonian theory of gravity can shed light on this dependence: The centripetal force on the star is given by its gravitational attraction force towards the center. Equating these two forces, one obtains [1]

$$\frac{mv(r)^2}{r} = \frac{GM(r)m}{r^2} \quad \Leftrightarrow \quad v(r) = \sqrt{\frac{GM(r)}{r}} \tag{1.1}$$

with Newton's gravitational constant G and the total enclosed mass $M(r)$ within the radius r, calculated from the mass density in the galaxy. Given the density function, one can obtain the rotation curve and vice versa. Let us assume that the galaxy only consists of visible matter. When r approaches the radius of the galaxy as measured from luminous matter, the density is expected to drop to zero, $M(r)$ converges to a finite value and becomes independent of r, so we expect rotation curves to behave as $r^{-1/2}$ for large r.
Rotation curves can be obtained experimentally by measuring the redshift of, for example, the 21 cm hydrogen line [2, 3]. In many galaxies the rotation curves are found to increase very slowly or form plateaus at large r [4]. In any case, they do not decrease as $r^{-1/2}$ at large distances, see figure 1.1, so these results contradict the predictions.

Of course this quick argument was based on Newtonian gravity and symmetry assumptions, but there are other situations in which measurements indicate that there seems to be more gravitating matter than expected. For example, already in the year 1933, Zwicky studied the dynamics of the Coma Cluster and concluded that its density, averaged over the entire cluster, is larger by a factor of at least 400 when compared to observations of visible matter [6]. Gravitational lensing,

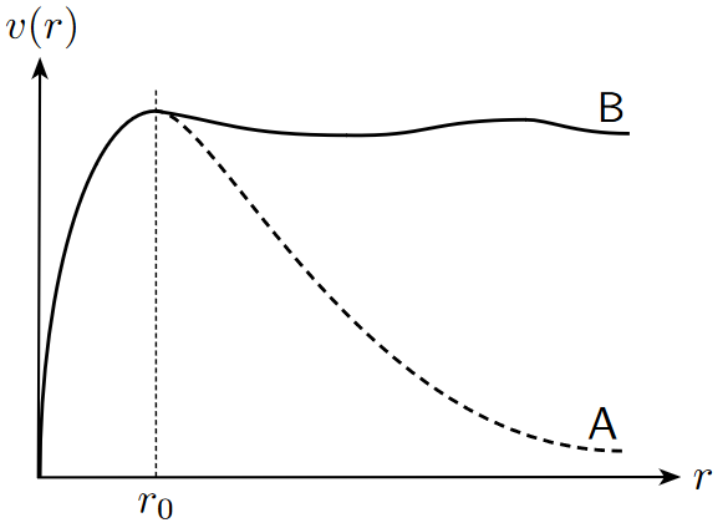

Figure 1.1: Sketch of a typical galaxy rotation curve. The dashed line A shows the decrease $\sim r^{-1/2}$ from the predictions while the solid line B represents a rotation curve as obtained from observations. Here, r_0 denotes the radius of the galaxy as defined by visible matter. This image has been adopted from [5].

i.e. the distortion of images due to light deflection by large masses, provides us with a similar clue: The strengths of these distortions indicate that there must be more gravitating matter than the one that is visible [7].
Since these and many more independent experiments come to the conclusion that there is some form of 'missing mass' which cannot be detected from electromagnetic measurements, it is reasonable to postulate a new type of gravitating matter which is called 'dark matter' (DM), as popularized by Zwicky [7]. In modern cosmological models, the contribution of DM to the total energy of the universe is estimated to be about 27 % while baryonic matter only contributes around 5 % [8]. Many different DM models have been proposed throughout the years, but the nature of DM is still an active field of research as summarized in [9]. In section 2.1 we will present two popular rather simple models, namely cold collisionless dark matter (CDM) and self-interacting dark matter (SIDM) and discuss what DM density spikes are.
It is certainly worth noting that there might also be other explanations of the observations described above like modified gravity theories. This thesis, however, assumes GR to be sufficiently accurate and attributes the missing mass problem to the existence of DM.

1.2 Black holes and black hole shadows

In 1915, Einstein published his full theory of GR. The first exact solution to the theory's fundamental set of equations, the Einstein field equations which determine the geometry of spacetime, was found by Schwarzschild soon after in 1916. [10]. His solution is nowadays called the Schwarzschild solution. It describes gravity in the vacuum around a static spherically symmetric mass distribution or a point mass. It turns out that the Schwarzschild solution contains a point-shaped singularity. A singularity can be intuitively thought of as a region where the spacetime geometry 'breaks down' or is not 'well-behaved'. Around the singularity there is a region from which no classical particle can ever escape [11]. Leaving aside the proper technical definitions, such a region is nowadays called a black hole (BH) and its boundary is referred to as an event horizon. This terminology is meaningful as an observer would simply see a black spot at the BH's position since its strong gravitational pull even traps photons, making everything inside the event horizon unobservable from the outside. Although Schwarzschild used different terminology, he had discovered BHs as a prediction of GR. For a long time, BHs were seen as a purely mathematical solution that is not realized in nature [12, 13]. In 1939, Oppenheimer and Snyder found that a BH might be able to form from the gravitational collapse of a star at the end of its lifetime [14], therefore providing a possible mechanism through which BHs could in fact form in nature. Bolton found in 1972 that observations of the X-ray source Cygnus X-1 were consistent with the existence of a BH as its companion [15].

Today we have plenty of experimental evidence that BHs are indeed physical reality and that they come in at least two groups defined by the BH's masses: The first group consists of stellar-mass BHs with approximately 3 to 100 solar masses and the second group is made up of supermassive BHs (SMBHs) with much larger masses of around 10^5 to 10^{10} solar masses [16]. Even though the origin of SMBHs is still being debated [17], there is evidence for their existence at the center of many, if not all, sufficiently large galaxies [18], including the Milky Way (MW) and Messier 87 (M87), a galaxy estimated to be located about 16.8 Mpc away from the MW [19]. These massive objects suspected to be BHs are called Sagittarius A* (Sgr A*) and M87* for the MW and M87*, respectively. The two names have appeared in the media a lot recently as the Event Horizon Telescope (EHT) collaboration has been able to produce pictures of these systems [20, 21]. These images can be found in figure 1.2. They show a dark region surrounded by a bright ring. The dark spot corresponds to the position of the BH and the ring is caused by an accretion disk, i.e. a mostly flat accumulation of material which moves around the BH and emits radiation along its way [22].

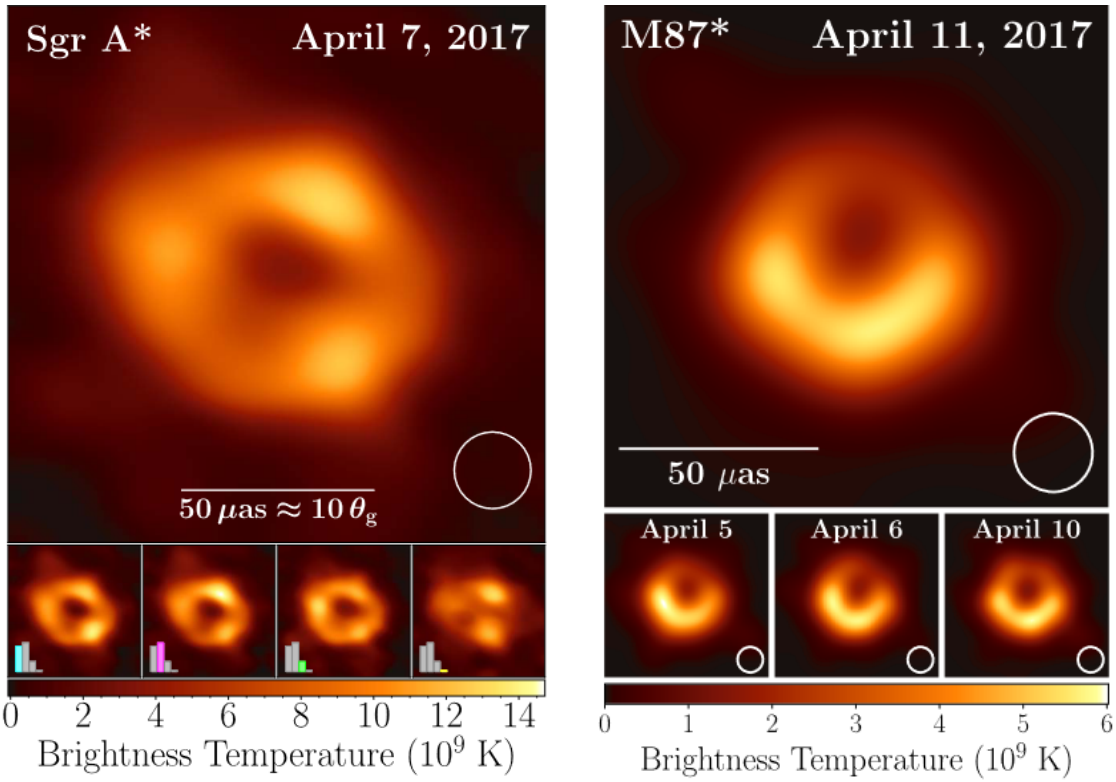

Figure 1.2: EHT images of Sgr A* (left) and M87* (right). The figures are taken from [20] and [21].

To be more precise, the dark part in the middle of such a picture does not show the BH's singularity which is unobservable, but its so-called BH shadow. The shadow of a BH is the part of an observer's field of view that remains completely black even if the line of sight points directly at the BH and if light sources are positioned everywhere except between the observer and the BH [23]. A BH shadow has non-zero extent which is a consequence of the bending of light around a BH, as described by GR. Photons emitted in directions pointing too close to the singularity will eventually be captured by the BH and not reach the observer. On the other hand, photons on trajectories sufficiently far away from the singularity can escape from the gravitational pull and possibly be detected by the observer. Each detected photon is seen as a bright spot on the observer's sky while the absence of photons from a particular direction leaves the corresponding point on the observer's sky black. A useful illustration of the situation is shown in figure 1.3. We will come back to the formation of BH shadows and define them in a more technical way in section 3.4.

1.3 Black hole shadows as a probe of dark matter

DM is by definition coupled to the gravitational interaction and might form 'clouds' that are stabilized by their own gravity. These so-called DM halos are

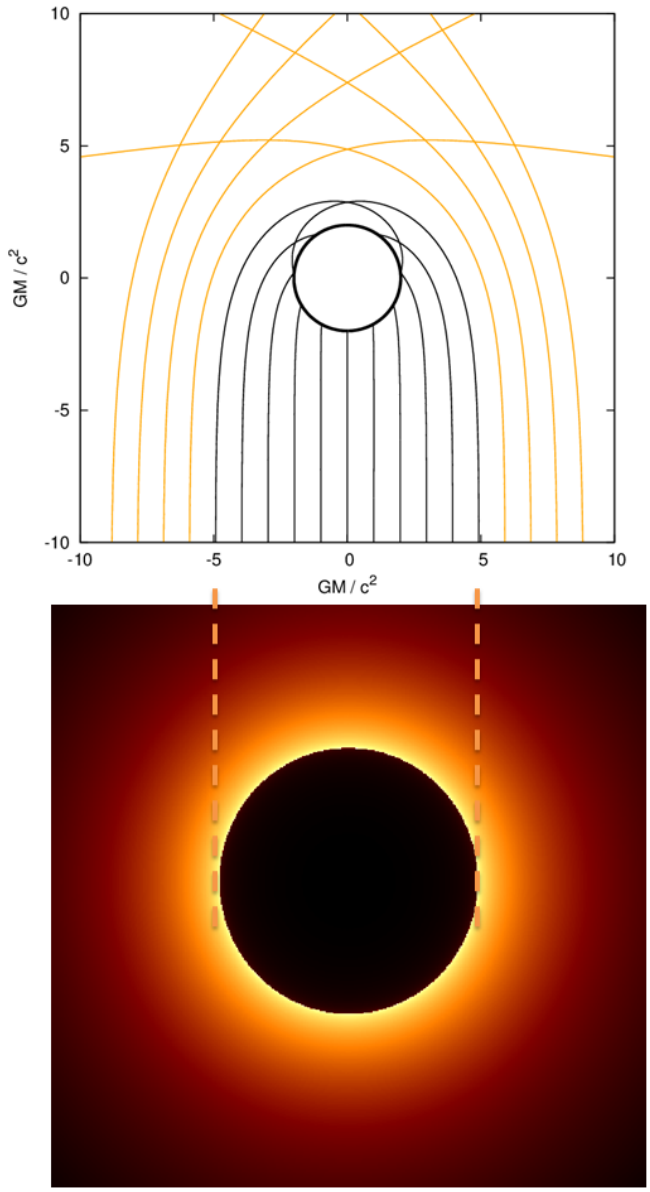

Figure 1.3: This image shows the basic principle behind the formation of a BH shadow. Some part of the observer's field of view remains black, even with light approaching the BH from various directions. The figure is taken from [24].

especially expected to exist around large masses like SMBHs due to their strong gravitational attraction. In these cases, the DM halos could form DM density spikes, i.e. highly increased DM densities near the BHs. We will discuss density spikes in more detail in section 2.1.3. Since the geometry of spacetime depends on the distribution of mass, energy and momentum in the system, it will be affected by the mass provided by the DM halo in addition to the BH. The changed geometry, in turn, results in deformed photon trajectories which should also lead to a different BH shadow compared to the one observed in the case without DM. The more DM the halo contains, the stronger the effect on the BH shadow

should be. Now the idea is to use a DM model, predict the properties of the halo it would form around a BH, calculate the movement of photons in the BH+DM halo system and hence predict the BH shadow one would observe. Different DM models might lead to different BH shadows and the hope is that the comparison between the predicted and the experimentally observed BH shadows can rule out some DM models. This would bring humanity closer to understanding the particle physical properties of DM.
In our work we covered the theoretical part of such a study of DM by modeling ten different hypothetical DM halos around the two BHs Sgr A* and M87* and calculating the resulting BH shadows of the combined systems.

1.4 Structure of this thesis

This thesis is organized as follows: In chapter 2, we will collect a couple of results from DM models and GR. They are not specific to our research, but will be useful in chapter 3 where we present the method for our BH shadow calculations in detail, including the modeling of the DM halo densities, a derivation of a suitable class of spacetimes and an explanation on how precisely different photon trajectories lead to an image of a BH shadow. Chapter 4 presents and discusses the results for the DM densities and the BH shadows from our calculations, shows a method to estimate the width of a BH shadow, addresses the uncertainties and limitations of our method and comments on the measurability of the DM effects in our results. Finally, a summary and an outlook are given in chapter 5.

2 Theoretical preliminaries

2.1 Dark matter models

In this section we will give a short overview of different DM models. We restrict ourselves to the models underlying our research, so this presentation is of course far from complete. A useful summary of DM candidates is given in [7].

2.1.1 Cold collisionless dark matter

Among all DM models, the CDM model is probably the most common and can be found in the standard description of cosmology, the ΛCDM model. There it successfully serves the purpose of explaining observations on large scales [25]. The CDM model assumes that DM consists of individual particles which move slowly compared to the speed of light ('cold') and do not scatter with one another ('collisionless'). Using these assumptions, Navarro, Frenk and White (NFW) ran simulations of a CDM halo (without a BH). Their famous result is that its mass density distribution ρ can be well described by a spherically symmetric profile of the form [26]

$$\rho_{\mathrm{NFW}}(r) = \frac{\rho_0}{\frac{r}{r_0}\left(1+\frac{r}{r_0}\right)^2} \tag{2.1}$$

where r is the distance from the halo's center. ρ_0 and r_0 (not to be confused with r_0 in figure 1.1) are positive constants of the dimensions density and length, respectively, that need to be fitted to the concrete system at hand. This so-called NFW profile has the property $\rho(r) \sim r^{-1}$ for $0 < r \ll r_0$, thereby forming a 'cusp' in the center of the system. For $r \gg r_0$, on the other hand, $\rho(r) \sim r^{-3}$.

2.1.2 Self-interacting dark matter

SIDM is a label given to all DM models in which there exist individual DM particles that can scatter with one another. Here the term 'scatter' is supposed to be understood in a very general sense. How precisely these self-interactions are implemented in theory varies from model to model, see for example the Jeans and the self-coupled scalar models [27].
One way to motivate the possibility of DM self-interactions is the following: Astrophysical observations of galaxies and galaxy clusters on various scales show that their density profiles in the inner regions are actually lower and flatter than expected from the CDM approach [28]. Such a flat density profile in the center is called a density 'core'. The discrepancy between observations preferring a core

or a cusp is summarized by the term 'core-cusp problem'. Figure 2.1 visualizes the need for a density core from observations of rotation curves.

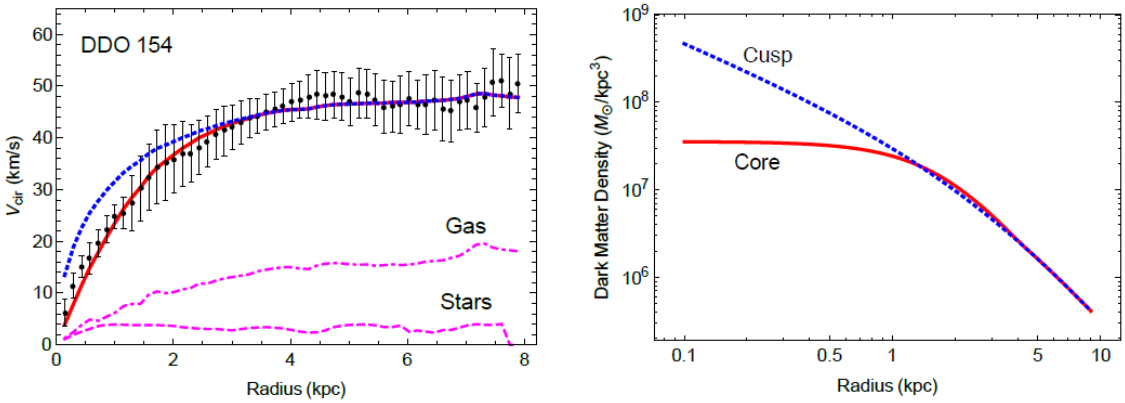

Figure 2.1: The rotation curve of the dwarf galaxy DDO 154 as constructed from observations (black dots) together with two fits corresponding to a density cusp (blue) and a density core (red). The cored density leads to a much better fit of the observed rotation curve. The plots are taken from [27]. Please also note the references therein for the origin of the shown data.

In order to form a density core from a cusp, there should be some mechanism that allows DM particles to be removed from the center and fed into the outer parts of the DM halo. DM scattering is one way to achieve this as shown in simulations [29]. Intuitively, one way to think about this effect is the following: In the center where the density is expected to be high compared to other parts of the halo, DM self-interactions are much more likely to occur. Assuming random scattering angles, more particles will be kicked out of the center since there is a larger solid angle available for a particle to move out rather than in. This depletes the center and decreases its DM density.

2.1.3 Dark matter density spikes

Usually, CDM and SIDM are models for a DM halo without any further effects. However, if, as is expected in reality, the halo has been formed by accretion onto a BH one should think about how the presence of the BH changes the DM density. This issue is addressed in [30]. The authors assume that a DM halo with a fixed density profile is given and that there is a very small seed BH in the halo's center. The BH will accrete matter from the halo and grow. Assuming that this growth progresses adiabatically, an initial profile behaving as $\rho \sim r^{-\Gamma}$ near the center will lead to an altered density $\rho \sim r^{-\gamma}$ near the center after the

growth of the BH. The new exponent γ is related to the initial one, Γ, by [30]

$$\gamma = \frac{9 - 2\Gamma}{4 - \Gamma} \quad . \tag{2.2}$$

From equation (2.2) it is not hard to verify that γ increases monotonically with Γ and that $\gamma \geq \Gamma$ for $0 < \Gamma < 4$. The first property means that the steeper the initial density profile, the steeper the final one. The second statement tells us that the final profile is always at least as steep as the one before the BH grew. Phrased differently, after the BH growth the density increases much faster the closer one gets to the BH. This increase in density near the BH is called a DM density spike and its density profile may be written as

$$\rho_{\text{spike}}(r) = \rho_{\text{sp}} \left(\frac{r_{\text{sp}}}{r} \right)^{\gamma} \quad , \quad 0 < r \leq r_{\text{sp}} \tag{2.3}$$

with some fixed r_{sp}, the so-called spike radius, and a proportionality constant $\rho_{\text{sp}} = \rho_{\text{spike}}(r_{\text{sp}})$. Notice that the restriction $r \leq r_{\text{sp}}$ in equation (2.3) is needed because a density spike is only an adequate description close to the BH.

2.2 Technical description of black holes

In GR, spacetime is modeled as a smooth four-dimensional manifold M that is equipped with, among other structures, a Lorentzian metric g and its Levi-Civita connection [11]. Gravity emerges as a consequence of spacetime's curvature in this formulation. The Einstein field equations relate the energy and momentum content of the physical system at hand to the geometry of the underlying spacetime. In an arbitrary coordinate system the Einstein field equations may be expressed as [31]

$$R_{\mu\nu} - \frac{1}{2} R g_{\mu\nu} = \frac{8\pi G}{c^4} T_{\mu\nu} \quad , \quad \mu, \nu = 0, ..., 3 \tag{2.4}$$

where $R_{\mu\nu}$ is the (μ, ν)-component of the Ricci tensor with respect to g, R is the Ricci scalar, $g_{\mu\nu}$ is the (μ, ν)-component of the metric, G is Newton's gravitational constant, c is the speed of light in vacuum and $T_{\mu\nu}$ is the (μ, ν)-component of the energy-momentum tensor. One can see that the left-hand side contains geometric quantities and the right-hand side consists of the energy-momentum content of the system. Sometimes, the Einstein field equations are written with an additional summand $\Lambda g_{\mu\nu}$ on the left-hand side. The real number Λ is called the cosmological constant and is related to dark energy and the expansion of the universe. Since we will only study stationary systems at some arbitrary but fixed point in time, we will not take cosmological effects into account and neglect the summand with the cosmological constant in the Einstein field equations.

Since the Ricci tensor, the metric and the energy-momentum tensor are symmetric, we may restrict ourselves to $\mu \leq \nu$ and are left with ten coupled non-linear differential equations for the metric components. Naturally, they are really hard to solve so only very few analytical solutions exist and those make use of certain symmetries or simplifying assumptions.

A class of comparatively simple systems to study is the vacuum for which all densities, pressures and momenta vanish so that $T_{\mu\nu} = 0$ everywhere for all μ, ν. One such solution to the Einstein field equations is called a vacuum solution. Probably the simplest non-trivial vacuum solution is the Schwarzschild solution which we already mentioned in section 1.2. With respect to a chart (U, x), the Schwarzschild chart, the Schwarzschild metric at some point $p := x^{-1}(t, r, \theta, \varphi)$ is expressed as [31]

$$g_{\mu\nu}(p) = \begin{pmatrix} -\left(1 - \frac{r_S}{r}\right) & 0 & 0 & 0 \\ 0 & \left(1 - \frac{r_S}{r}\right)^{-1} & 0 & 0 \\ 0 & 0 & r^2 & 0 \\ 0 & 0 & 0 & r^2 \sin^2(\theta) \end{pmatrix}_{\mu\nu} \tag{2.5}$$

with $t \in \mathbb{R}$, $r \in \mathbb{R}^+ \setminus \{r_S\}$, $\theta \in (0, \pi)$ and $\varphi \in (0, 2\pi)$. $r_S = 2GM_{\mathrm{BH}}/c^2$ is the so-called Schwarzschild radius. It depends on $M_{\mathrm{BH}} \in \mathbb{R}_0^+$ which may be interpreted as a mass as will be clarified later in this section.
One immediately sees that the metric components exhibit singularities at the coordinates $r = 0$ and $r = r_S$. In order to decide whether those points are physical singularities or merely coordinate-singularities arising from the choice of chart, one has to study quantities that do not depend on the chosen coordinate system. One such quantity is the Kretschmann scalar $K := R^{\mu\nu\rho\sigma} R_{\mu\nu\rho\sigma}$ which is constructed by contracting all components of the Riemann tensor and is thus a true scalar: Its values may be expressed using coordinates but ultimately they do not depend on the coordinate system but only the actual points in spacetime. For the Schwarzschild solution (2.5), the Kretschmann scalar takes the form [32]

$$K(p) = \frac{12 r_S^2}{r^6} \quad . \tag{2.6}$$

with p as defined above. Notice how K is perfectly well-behaved at $r = r_S$. Hence, the hypersurface defined by the Schwarzschild radius does not stand out in any way in terms of geometry and we conclude that $r = r_S$ is a coordinate-singularity. However, K diverges to ∞ for $r \to 0^+$ which means that $r = 0$ is a physical singularity. The hypersurface of points with $r = r_S$ turns out to bound a region from which, once entered, no classical particle can escape and in this sense, it is not possible for two observers on opposite sides of the hypersurface

to 'communicate'. In other words, that hypersurface is an event horizon and the Schwarzschild solution describes a BH. Since the radius of the event horizon grows with M_{BH}, it is reasonable to interpret M_{BH} as the mass of the BH, as indicated above.

More generally, whenever a solution to the Einstein field equations exhibits "a region of spacetime causally disconnected from future infinity" [12], we speak of a BH solution. In fact, the Schwarzschild solution is only one example of a much bigger class of BH solutions. Another important example is the class of Kerr solutions, given by [32]

$$g_{\mu\nu}(\widetilde{p}) = \begin{pmatrix} -\left(1-\frac{r_S r}{\Sigma(r,\theta)}\right) & 0 & 0 & -\frac{r_S a \sin^2(\theta)}{\Sigma(r,\theta)} r \\ 0 & \frac{\Sigma(r,\theta)}{\Delta(r)} & 0 & 0 \\ 0 & 0 & \Sigma(r,\theta) & 0 \\ -\frac{r_S a \sin^2(\theta)}{\Sigma(r,\theta)} r & 0 & 0 & \Psi(r,\theta)\sin^2(\theta) \end{pmatrix}_{\mu\nu} \tag{2.7}$$

where $\widetilde{p} := \widetilde{x}^{-1}(t, r, \theta, \varphi)$ in so-called Boyer-Lindquist coordinates $\widetilde{x}$ and with the abbreviations $\Sigma(r,\theta) = r^2 + a^2\cos^2(\theta)$, $\Delta(r) = r^2 - r_S r + a^2$ and $\Psi(r,\theta) = r^2 + a^2 + \frac{r_S a^2 \sin^2(\theta)}{\Sigma(r,\theta)} r$. In addition to the BH M_{BH}, the Kerr metrics have an additional free parameter $a \in [-1,1]\, GM_{\mathrm{BH}}/c^2$ which can be interpreted as a measure of rotation of the BH and is thus called the spin parameter of the Kerr BH. In the case $a = 0$, the Kerr metric (2.7) reduces to the Schwarzschild metric (2.5).

The Schwarzschild and Kerr metrics will be helpful guidelines in section 3.2 where we will construct metrics for the systems we want to study, namely rotating BHs within DM halos.

2.3 Geodesic motion

In order to be able to compute BH shadows we need to understand how photons move in a given spacetime. It is a central postulate of GR that free particles move on geodesics with respect to the spacetime metric g. Here and in the following, calculations will be carried out with respect to a fixed but arbitrary chart (U, x) of M. In such local coordinates, a smooth curve $\gamma : I \to U$ from some real interval I into a subset of spacetime is a geodesic if it satisfies the geodesic equation [11]

$$\ddot{\gamma}^\alpha(\lambda) + \Gamma^\alpha_{\mu\nu}(\gamma(\lambda))\dot{\gamma}^\mu(\lambda)\dot{\gamma}^\nu(\lambda) = 0 \quad , \quad \alpha = 0,1,2,3 \tag{2.8}$$

for all $\lambda \in I$. The $\gamma^\alpha = x^\alpha \circ \gamma$ are the coordinate representations of the curve γ, $\Gamma^\alpha_{\mu\nu}$ are the Christoffel symbols of the Levi-Civita connection of g in the same

coordinates and a dot denotes a derivative with respect to the curve parameter.

The inner product of tangent vectors is conserved under parallel transport defined by the Levi-Civita connection, so all tangent vectors to a geodesic either have a negative, zero or positive inner product with themselves and we classify such curves as time-like, null and space-like, respectively [11]. If γ is the trajectory of a particle, γ is time-like if the particle is massive and null if the particle has zero mass like a photon [11]. In formulae, we have

$$g_{\mu\nu}(\gamma(\lambda))\dot{\gamma}^{\mu}(\lambda)\dot{\gamma}^{\nu}(\lambda) \begin{cases} < 0 \text{ for a massive particle} \\ = 0 \text{ for a massless particle} \end{cases} \tag{2.9}$$

for all $\lambda \in I$.

It will be convenient to identify conserved quantities along geodesics and this can be achieved by translating the mechanical problem into a Hamiltonian framework. To this end we first note that the equations (2.8) are precisely the Euler-Lagrange equations for a Lagrangian $\mathcal{L} : TM \to \mathbb{R}$ on the tangent bundle TM whose local canonical coordinate representation L with respect to x is given by

$$L(Q^0, ..., Q^3, V^0, ..., V^3) = \frac{1}{2} g_{\mu\nu}(x^{-1}(Q^0, ..., Q^3)) V^{\mu} V^{\nu} \quad . \tag{2.10}$$

The corresponding Hamiltonian $\mathcal{H} : T^*M \to \mathbb{R}$ on the cotangent bundle / phase space T^*M by virtue of the musical isomorphism induced by g has a local coordinate representation H that can be obtained from L by a Legendre transformation, resulting in

$$H(Q^0, ..., Q^3, P_0, ..., P_3) = \frac{1}{2} \overline{g}^{\mu\nu}(x^{-1}(Q^0, ..., Q^3)) P_{\mu} P_{\nu} \quad . \tag{2.11}$$

The functions $\overline{g}^{\mu\nu}$ are the component functions of the cometric $\overline{g}$ with respect to g that satisfy $\overline{g}^{\mu\nu} g_{\nu\rho} = \delta^{\mu}_{\rho}$ everywhere in U with δ being the Kronecker delta symbol. In this formalism, the equations of motion for γ are given by Hamilton's equations:

$$\begin{aligned} \dot{q}^{\mu}(\lambda) &= (\partial_{4+\mu} H)\,(q(\lambda), p(\lambda)) \quad , \quad \mu = 0, ..., 3 \quad , \\ \dot{p}_{\mu}(\lambda) &= -(\partial_{\mu} H)\,(q(\lambda), p(\lambda)) \quad , \quad \mu = 0, ..., 3 \quad . \end{aligned} \tag{2.12}$$

We write $(q, p) \equiv (q^0, ..., q^3, p_0, ..., p_3)$ for the coordinate representation of the lift of γ into T^*M with respect to the musical isomorphism. Again, these equations need to hold for all $\lambda \in I$.

2.4 Circular orbits around a Kerr black hole

An aspect that will be important for modeling the DM density profiles is how close particles can orbit a BH without falling into it. Consider a particle moving in a Kerr spacetime (2.7). In [33] it was shown that if the particle is massive, a bound circular orbit of Boyer-Lindquist radius r in the equatorial plane with $\theta = \pi/2$ is completely stable if and only if $r > r_{\text{ms, massive}}$ where

$$\begin{aligned} r_{\text{ms, massive}} &= \left[3 + Z_2 \pm \sqrt{(3 - Z_1)(3 + Z_1 + 2Z_2)}\right] \frac{GM_{\text{BH}}}{c^2} \quad , \\ Z_1 &= 1 + \sqrt[3]{1 - A^2}\left(\sqrt[3]{1 + A} + \sqrt[3]{1 - A}\right) \quad , \\ Z_2 &= \sqrt{3A^2 + Z_1^2} \quad , \\ A &= \frac{a}{GM_{\text{BH}}/c^2} \quad . \end{aligned} \tag{2.13}$$

$r_{\text{ms, massive}}$ is the radius of the marginally stable circular orbit, which means it separates the stable from the unstable orbits [34]. The choice of sign in equation (2.13) depends on whether the particle is in retrograde $(+)$ or prograde $(-)$ motion with the Kerr BH.
If a similar analysis is done for massless particles like photons, one finds that there are only two possible radii for circular orbits in the equatorial plane, given by [33, 35]

$$r_{\text{massless}} = 2\left[1 + \cos\left(\frac{2}{3}\arccos(\pm|A|)\right)\right]\frac{GM_{\text{BH}}}{c^2} \quad . \tag{2.14}$$

As before $(+)$ corresponds to retrograde and $(-)$ to prograde motion and A is defined as in equation (2.13). When the restriction of equatorial trajectories is lifted, photons can only move on trajectories of constant r between these two values [35].

Figure 2.2 visualizes the important radii from equations (2.13) and (2.14) by considering them as functions of the BH spin parameter a while fixing M_{BH}. The radii for prograde and retrograde orbits obviously coincide at $a = 0$ with a value of $6\,GM_{\text{BH}}/c^2$ for massive and $3\,GM_{\text{BH}}/c^2$ for massless particles. Independent of the particle mass, for increasing a, the prograde orbits have decreasing radii and this decrease becomes stronger at large a. In the case of retrograde motion, on the other hand, there is an almost linear increase. The main piece of information to keep in mind from this section is that prograde circular motion in the equatorial plane is more strongly affected by a large spin parameter than retrograde motion.

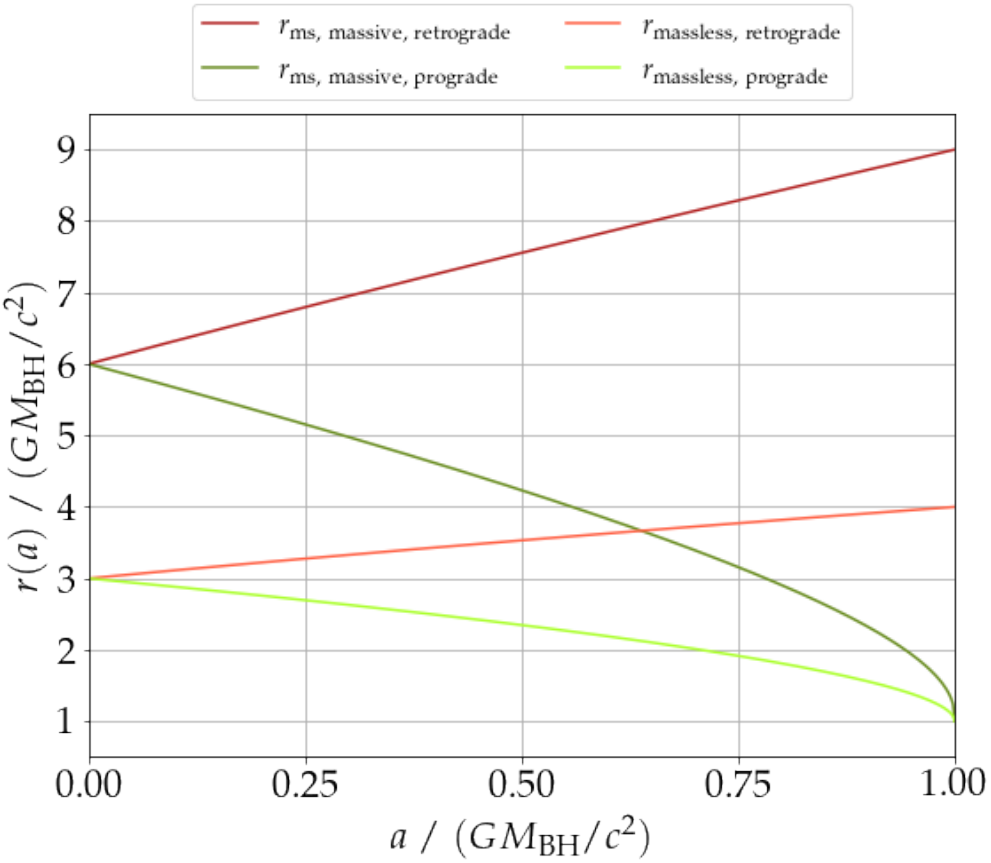

Figure 2.2: Radii of the discussed orbits around a Kerr BH of mass M_{BH} in dependence of the spin parameter a.

3 Method

3.1 Modeling the dark matter halos

For the halos around Sgr A* and M87*, we will use ten different spherically symmetric DM density profiles each: one NFW profile, four SIDM profiles for different interaction cross-sections and variants of these five profiles that include DM density spikes. The overall approach is the same for Sgr A* and M87*, the only difference will be the values of certain parameters in the models.

For the NFW profile, one only needs to provide ρ_0 and r_0. The values and their references can be found in table 3.1.

	$\rho_0/(M_\odot\,\mathrm{kpc}^{-3})$	r_0/kpc
Sgr A*	$1.936 \cdot 10^7$ [36]	17.46 [36]
M87*	$(4\pi)^{-1} \cdot 10^{7.51}$ [37]	128.4 [37]

Table 3.1: NFW parameters ρ_0 and r_0 that we are going to use for a CDM halo around Sgr A* and M87*.

For SIDM, we will follow the approach taken in [28] and make use of the Jeans model as also thoroughly described in [38] to model the self-interactions: In short, one assumes DM particles to constitute an ideal gas, so perfectly elastic self-interactions between its constituents are allowed. From the ideal gas law and the assumption of hydrostatic equilibrium between pressure and gravity one can derive [28]

$$\sigma_0^2 \left(\Delta(\ln \circ \rho)\right)(r) = -4\pi G \rho(r) \tag{3.1}$$

where Δ is the Laplace operator on 3D Euclidean space. This equation relates the DM density $\rho(r)$ at r to the one-dimensional velocity dispersion σ_0 of the DM particles which encodes their relative velocities. As mentioned in section 2.1.1, the NFW profile has been seen in experiments to be an appropriate description of DM on large scales, so it will be kept with its parameters unchanged outside of a specific radius r_m, the matching radius. It is determined by the requirement that there is only one expected self-interaction of DM particles over the entire lifetime t_age of the system. We are going to make the simplifying assumption that the DM self-interaction cross sections per unit mass σ/m are velocity-independent. They can then be shown to depend on the matching radii r_m like [28]

$$\frac{\sigma}{m} = \frac{\sqrt{\pi}}{4\sigma_0 \rho(r_\mathrm{m}) t_\mathrm{age}} \quad . \tag{3.2}$$

Within r_m, the interactions are not negligible and are taken into account by using a specific solution ρ_{Jeans} to equation (3.1) for $r < r_m$ in the halo. For this solution, the constants of integration are chosen such that $\rho_{\text{Jeans}}(r_m) = \rho_{\text{NFW}}(r_m)$ and $M_{\text{Jeans}}(r_m) = M_{\text{NFW}}(r_m)$ which ensures continuity of the whole density function and that the mass within r_m is the same as if it were described by an NFW profile. The lifetime of the system will be set to $t_{\text{age}} = 10\,\text{Gyr}$ as in [28]. In summary, our SIDM density profile is given by

$$\rho_{\text{SIDM}}(r) = \begin{cases} \rho_{\text{Jeans}}(r) & 0 < r < r_m \\ \rho_{\text{NFW}} & r \geq r_m \end{cases} \quad . \tag{3.3}$$

Motivated by the expected order of magnitude for the cross section per unit mass [27], we use $\sigma/m = 0.01$, 0.1, 1 and $5\,\text{cm}^2\,\text{g}^{-1}$ and call the corresponding density profiles SIDM 1, SIDM 2, SIDM 3 and SIDM 4. How precisely those are obtained is explained in [38]. [39] provides the code to do the calculations.

In order to take the BH in the center of the DM halo into account, within some spike radius r_{sp}, we introduce a density spike into the profiles (2.1) and (3.3) by hand. For CDM obeying an NFW profile, we have $\rho(r) \sim r^{-1}$ close to the center and can set $\Gamma = 1$ in equation (2.2) so that $\gamma = 7/3$. For SIDM, we set $\gamma = 7/4$ as also done in [40]. The NFW and SIDM profiles with the spikes are hence given by

$$\rho_{\text{spiked NFW}}(r) = \begin{cases} \rho_{\text{spike}}(r) \text{ with } \gamma = 7/3 & 0 < r < r_{\text{sp, spiked NFW}} \\ \rho_{\text{NFW}}(r) & r \geq r_{\text{sp, spiked NFW}} \end{cases} , \tag{3.4}$$

$$\rho_{\text{spiked SIDM}}(r) = \begin{cases} \rho_{\text{spike}}(r) \text{ with } \gamma = 7/4 & 0 < r < r_{\text{sp, spiked SIDM}} \\ \rho_{\text{Jeans}}(r) & r_{\text{sp, spiked SIDM}} \leq r < r_m \\ \rho_{\text{NFW}}(r) & r \geq r_m \end{cases} . \tag{3.5}$$

The implicit assumption that $r_{\text{sp, spiked SIDM}} < r_m$ is justified because the spike radius characterizes the DM spike with a very large DM density while the matching radius, by definition, lies at a radius with a rather low density. Again, the free parameters are determined by continuity requirements and the spiked SIDM density profiles are labeled spiked SIDM 1, spiked SIDM 2, spiked SIDM 3 and spiked SIDM 4 for the four different cross sections as before.
The question that remains is how to determinate the spike radii. In [41] and [42], it is suggested to fix r_{sp} (standing for $r_{\text{sp, spiked NFW}}$ or $r_{\text{sp, spiked SIDM}}$ here) by the requirement that the enclosed mass within $5\,r_{\text{sp}}$ is twice the mass of the central BH:

$$4\pi \int_0^{5\,r_{\text{sp}}} r^2 \rho(r) \mathrm{d}r = 2M_{\text{BH}} \quad . \tag{3.6}$$

To emphasize, the density ρ in this equation is taken to be given by equation (3.4) or (3.5). For a given M_{BH}, the existence and uniqueness of r_{sp} is guaranteed by the observation that the function $R \mapsto \int_0^R r^2 \rho(r) \mathrm{d}r$ is continuous, strictly monotonically increasing and has $\mathbb{R}^+$ as its image. Solving equation (3.6) for r_{sp} needs to be done numerically. We use the values $M_{\mathrm{BH}} = 4.3 \cdot 10^6 \, M_\odot$ for Sgr A* [43] and $M_{\mathrm{BH}} = 6.5 \cdot 10^9 \, M_\odot$ for M87* [44].

3.2 Deriving a metric of a spacetime of a black hole in a dark matter halo

In order to study shadows of BHs which are surrounded by DM halos, we need to understand how photons move in these systems. Since gravity near the BHs is strong, this requires a general relativistic treatment. The goal of this section is to derive a spacetime metric which describes a DM halo containing a possibly rotating BH in its center, so that later on the photon paths can be calculated with the geodesic equation. The derivation of the metric is done in a couple of steps: First, a metric for a spherically symmetric and stationary DM halo is constructed. Then, we will derive a modification of this result which additionally accounts for a Schwarzschild BH. In the next step, this metric will be generalized to allow for rotating BHs. Finally, a small retroactive modification will be done to the DM densities.

3.2.1 Geometry of a dark matter halo

For the moment, let us restrict to a system consisting only of a spherically symmetric and stationary DM halo. The goal is to find a general relativistic description of a spacetime with such a halo. More concretely, given a density profile ρ in three-dimensional Euclidean space, we would like to find a way to obtain a corresponding spacetime metric $\hat{g}$. We will derive a few results in [45], but present an alternative approach using the geodesic equation.

Consider a massive test particle moving through the halo on a circular orbit of radius R, subject to the halo's gravitational pull only. We assume that the circle's center coincides with the halo's center. Since, for now, the DM halo is assumed to be static and spherically symmetric, there exists a chart $(U, \hat{x})$ such that the metric components at a point $\hat{p} := \hat{x}^{-1}(t, r, \theta, \varphi)$ with respect to that chart have the form [31]

$$\hat{g}_{\mu\nu}(\hat{p}) = \mathrm{diag}\left(-F(r), G(r)^{-1}, r^2, r^2 \sin^2(\theta)\right)_{\mu\nu} \tag{3.7}$$

for some functions F and G. Here we have $t \in (-\infty, \infty)$, $r \in J$ where $J \subseteq (0, \infty)$, $\theta \in (0, \pi)$ and $\varphi \in (0, 2\pi)$. We make another assumption by requiring $G = F$

everywhere. This condition has not been imposed in [45]. In later parts of section 3.2, we will mainly follow [46] and [47] where $G = F$ is assumed, so we will do the same at this point already to simplify the following arguments. In this case we have the ansatz

$$\hat{g}_{\mu\nu}(\hat{p}) = \operatorname{diag}\left(-F(r), F(r)^{-1}, r^2, r^2\sin^2(\theta)\right)_{\mu\nu} \tag{3.8}$$

and $F(r)$ is the only unknown quantity that we need to find.
Let $\lambda \mapsto (t(\lambda), r(\lambda), \theta(\lambda), \varphi(\lambda)) := (\gamma^0(\lambda), \gamma^1(\lambda), \gamma^2(\lambda), \gamma^3(\lambda))$ be a parametrization of the particle's trajectory γ in $\hat{x}$ coordinates. Due to spherical symmetry, we can assume without loss of generality that the circular orbit lies on the 'equator', i.e. we have $\theta(\lambda) = \pi/2$ and $r(\lambda) = R$ for all λ. In particular, we have $\dot{\theta}(\lambda) = \dot{r}(\lambda) = 0$ for all λ. We calculate the Christoffel symbols of the Levi-Civita connection with respect to $\hat{g}$ by [48]

$$\Gamma^{\lambda}_{\mu\nu} = \frac{1}{2}\overline{\hat{g}}^{\lambda\sigma}\left(\frac{\partial \hat{g}_{\mu\sigma}}{\partial \hat{x}^{\nu}} + \frac{\partial \hat{g}_{\nu\sigma}}{\partial \hat{x}^{\mu}} - \frac{\partial \hat{g}_{\mu\nu}}{\partial \hat{x}^{\sigma}}\right) \tag{3.9}$$

where $\frac{\partial \hat{g}_{\mu\sigma}}{\partial \hat{x}^{\nu}} = \left(\partial_{\nu}\left(\hat{g}_{\mu\sigma} \circ \hat{x}^{-1}\right)\right) \circ \hat{x}$ and find that the geodesic equation (2.8) for γ reduces to

$$\ddot{t}(\lambda) = 0 \quad , \tag{3.10}$$

$$F'(R)(\dot{t}(\lambda))^2 - 2R(\dot{\varphi}(\lambda))^2 = 0 \quad , \tag{3.11}$$

$$\ddot{\varphi}(\lambda) = 0 \quad . \tag{3.12}$$

From the first and third equation, we conclude $\dot{t}(\lambda) = \Xi(R)$ and $\dot{\varphi}(\lambda) = \omega(R)$ for all λ where $\Xi(R)$ and $\omega(R)$ are constant with respect to the curve parameter λ but might depend on R. Since we look at the motion of a massive particle, γ is a time-like curve and we can arrange such that, for all λ, we have $g_{\mu\nu}(\gamma(\lambda))\dot{\gamma}^{\mu}(\lambda)\dot{\gamma}^{\nu}(\lambda) = -1$. This equation is equivalent to $\Xi(R)^2 = (R^2\omega(R)^2 + 1)/F(R)$ which we can substitute into equation (3.11) to obtain

$$F'(R)\frac{R^2\omega(R)^2 + 1}{F(R)} - 2R\omega(R)^2 = 0 \quad . \tag{3.13}$$

This equation can be rearranged into

$$\frac{F'(R)}{F(R)} = \frac{2}{R}\frac{R^2\omega(R)^2}{R^2\omega(R)^2 + 1} \quad . \tag{3.14}$$

In this form the differential equation for $F(R)$ can formally be solved by integration. In agreement with the ansatz (3.8) and the signature of $\hat{g}$, we take $F(R)$ to be positive so that we do not need absolute values. We obtain

$$\ln\left(F(R)\right)\Big|_{R_1}^{R_2} = \int_{R_1}^{R_2}\frac{2}{R}\frac{R^2\omega(R)^2}{R^2\omega(R)^2 + 1}\mathrm{d}R \quad . \tag{3.15}$$

The integral, however cannot be solved explicitly yet because it is not clear how $\omega(R)$ depends on R. This is where we unfortunately need some hand-waving arguments to build the connection: We identify $R^2\omega(R)^2/(R^2\omega(R)^2+1)$ from equation (3.15) with $v(R)^2/c^2$ where $v(R)$ is the velocity of the particle as in equation (1.1). This step is not as arbitrary as it may seem because $R^2\omega(R)^2/(R^2\omega(R)^2+1)$ is proportional to $(R\omega(R))^2$ where ω can be seen as the angular velocity of the particle. We also have $R^2\omega(R)^2/(R^2\omega(R)^2+1) \in [0,1)$ which is required for the square of the velocity of a massive particle in units of c^2.
After this identification we can rewrite equation (3.15) as

$$\ln\left(F(R)\right)\Big|_{R_2}^{R_1} = -\frac{2G}{c^2}\int_{R_1}^{R_2}\frac{M(R)}{R^2}\mathrm{d}R \quad . \tag{3.16}$$

After taking the limit $R_2 \to \infty$, requiring $\lim_{R_2\to\infty} F(R_2) = 1$ for asymptotic flatness, exponentiating and renaming variables for convenience we arrive at

$$F(r) = \exp\left\{-\frac{2G}{c^2}\int_r^\infty \frac{M(r')}{r'^2}\mathrm{d}r'\right\} \quad . \tag{3.17}$$

One should think briefly if the expressions in equation (3.17) are all well-defined. The enclosed mass function M will be guaranteed to be well-defined for our purposes because we will only consider density profiles with an asymptotic behavior $\rho(r) \sim r^{-\gamma}$ with $\gamma < 3$ as $r \to 0^+$. For the convergence of the improper integral, we note that we will only use density functions that, outside of some radius, have the shape of an NFW profile whose enclosed mass function $r' \mapsto M(r')$ diverges logarithmically as $r' \to \infty$. The integral is therefore of the form $\int_{x_0}^\infty \ln(1+x)/x^2\mathrm{d}x$ which can be shown to converge. So mathematically, the result (3.17) is well-defined.
For numerical purposes it is more convenient to manipulate the result further by integration by parts, inserting the definition for the enclosed mass $M(r')$ and using its asymptotic behavior:

$$F(r) = \exp\left\{-\frac{8\pi G}{c^2}\left[\frac{1}{r}\int_0^r r'^2\rho(r')\mathrm{d}r' + \int_r^\infty r'\rho(r')\mathrm{d}r'\right]\right\} \tag{3.18}$$

In this form, we can easily make a small cross-check: If the DM density ρ vanishes everywhere, we have $F \equiv 1$. Thus, we have recovered the Minkowski metric with spherical spatial coordinates, as required.

3.2.2 Including a Schwarzschild black hole

Once the metric of the DM halo is known it can be extended to include a Schwarzschild BH. Following [46], the idea is that a Schwarzschild spacetime

is a vacuum solution of the Einstein equations, meaning that its corresponding energy-momentum tensor is zero everywhere, and therefore the spacetime of the DM halo and the spacetime of a Schwarzschild BH within the same DM halo should have the same energy-momentum tensors.
In order to make this concrete, let $\hat{g}, \hat{R}, \hat{T}$ and $\widetilde{g}, \widetilde{R}, \widetilde{T}$ denote the metrics, Ricci tensors and scalars and energy-momentum tensors of the spacetimes with the DM halo alone and with the DM halo around a Schwarzschild BH, respectively. Then the mixed contravariant/covariant Einstein equations for these spacetimes read

$$\hat{R}^{\mu}{}_{\nu} - \frac{1}{2}\hat{R}\delta^{\mu}{}_{\nu} = \hat{T}^{\mu}{}_{\nu} \quad , \tag{3.19}$$

$$\widetilde{R}^{\mu}{}_{\nu} - \frac{1}{2}\widetilde{R}\delta^{\mu}{}_{\nu} = \widetilde{T}^{\mu}{}_{\nu} \quad . \tag{3.20}$$

Using the equality of energy-momentum tensors as discussed before we obtain

$$\hat{R}^{\mu}{}_{\nu} - \frac{1}{2}\hat{R}\delta^{\mu}{}_{\nu} = \widetilde{R}^{\mu}{}_{\nu} - \frac{1}{2}\widetilde{R}\delta^{\mu}{}_{\nu} \quad . \tag{3.21}$$

For the moment we still assume both spacetimes to be spherically symmetric and static. This allows us to make an ansatz as in equation (3.8) and we can write

$$\widetilde{g}_{\mu\nu}(\widetilde{p}) = \operatorname{diag}\left(-f(r), f(r)^{-1}, r^2, r^2\sin^2(\theta)\right)_{\mu\nu} \tag{3.22}$$

at some point $\widetilde{p} := \widetilde{x}^{-1}(t, r, \theta, \varphi)$ for a suitable chart map $\widetilde{x}$. The new metric function $f(r) := F(r) + F_{\mathrm{c}}(r)$ includes a correction term $F_{\mathrm{c}}(r)$ due to the BH.
Computing the components of the Ricci tensors from our ansatz, equation (3.21) reduces to the following two equations:

$$\frac{F_{\mathrm{c}}'(r)}{r} + \frac{F_{\mathrm{c}}(r)}{r^2} = 0 \quad , \tag{3.23}$$

$$\frac{F_{\mathrm{c}}''(r)}{2} + \frac{F_{\mathrm{c}}'(r)}{r} = 0 \tag{3.24}$$

By differentiation, the second one can be shown to follow from the first, so we only need to solve the first equation. Its general solution is

$$F_{\mathrm{c}}(r) = \frac{\kappa}{r} \tag{3.25}$$

with an arbitrary constant $\kappa \in \mathbb{R}$. It can be fixed by demanding that for no DM (or, equivalently, $F \equiv 1$ as mentioned before), $\widetilde{g}$ should turn into the Schwarzschild solution with a BH mass M_{BH}. From

$$\begin{aligned} F(r) + F_{\mathrm{c}}(r) &= 1 + \frac{\kappa}{r} \\ &= 1 - \frac{2GM_{\mathrm{BH}}}{c^2 r} \end{aligned} \tag{3.26}$$

we find $\kappa = -2GM_{\mathrm{BH}}/c^2$ so that

$$f(r) = F(r) - \frac{2GM_{\mathrm{BH}}}{c^2 r} \tag{3.27}$$

and the pure DM halo spacetime is recovered for $M_{\mathrm{BH}} = 0$, exactly as needed.

3.2.3 Introducing a spin parameter

At this point, the metric is still spherically symmetric and static. These symmetry assumptions will need to be relaxed to axial symmetry if rotating BHs are supposed to be considered. There is a standard, albeit debatable, procedure to turn a spherically symmetric BH metric into an axially symmetric metric: the Newman-Janis algorithm. It was first proposed in [49] as a sequence of purely mathematical steps to construct the Kerr metric from the Schwarzschild metric without any physical justification. Throughout the years, a lot of work has been done to better understand why and under which conditions the algorithm produces physical metrics. An overview is given in [50].
We follow [46] and apply the Newman-Janis algorithm to the metric (3.22) to obtain the metric of a rotating BH in a DM halo, given by

$$g_{\mu\nu}(p) = \begin{pmatrix} -\left[1 - \frac{r^2 - f(r)r^2}{\Sigma(r,\theta)}\right] & 0 & 0 & -\frac{(r^2 - f(r)r^2)a\sin^2(\theta)}{\Sigma(r,\theta)} \\ 0 & \frac{\Sigma(r,\theta)}{\Delta(r)} & 0 & 0 \\ 0 & 0 & \Sigma(r,\theta) & 0 \\ -\frac{(r^2 - f(r)r^2)a\sin^2(\theta)}{\Sigma(r,\theta)} & 0 & 0 & \Phi(r,\theta)\sin^2(\theta) \end{pmatrix}_{\mu\nu} \tag{3.28}$$

at $p := x^{-1}(t, r, \theta, \varphi)$ with respect to some new chart map x. $f(r)$ is the metric component as in equation (3.27), $a \in [-1, 1]\, GM_{\mathrm{BH}}/c^2$ is interpreted as the BH spin parameter, $\Sigma(r,\theta) = r^2 + a^2\cos^2(\theta)$ as in equation (2.7), $\Delta(r) = r^2 f(r) + a^2$ and $\Phi(r,\theta) = \left[(r^2 + a^2)^2 - a^2\Delta(r)\sin^2(\theta)\right]/\Sigma(r,\theta)$. The negative signs in the off-diagonal terms were dropped by accident in [46], but apart from that, our result agrees with theirs. One can quickly see that the metric (3.28) reduces to (3.22) for $a = 0$, as required. For later use, by inverting the matrix above, the components of the cometric are found to be

$$\overline{g}^{\mu\nu}(p) = \begin{pmatrix} -\frac{\Phi(r,\theta)}{\Delta(r)} & 0 & 0 & -\frac{a(r^2 - f(r)r^2)}{\Sigma(r,\theta)\Delta(r)} \\ 0 & \frac{\Delta(r)}{\Sigma(r,\theta)} & 0 & 0 \\ 0 & 0 & \frac{1}{\Sigma(r,\theta)} & 0 \\ -\frac{a(r^2 - f(r)r^2)}{\Sigma(r,\theta)\Delta(r)} & 0 & 0 & \frac{a^2\cos^2(\theta) + r^2 f(r)}{\sin^2(\theta)\Sigma(r,\theta)\Delta(r)} \end{pmatrix}_{\mu\nu} . \tag{3.29}$$

3.2.4 Restricting the dark matter halo's size

From a physical point of view, there should not be any DM particles inside the radius of the prograde marginally stable circular orbit of a massive particle

(recall section 2.4) since we are only going to study stationary systems. This means that the DM density should be set to zero within that radius which we will call r_{min} here instead of $r_{\text{ms, massive, prograde}}$. The calculations for r_{min} for the different BHs, spin parameters and DM halos have been carried out by Jorden Roberts who worked with us on the project. He used the method of effective potentials and found that all DM halos have a negligible contribution to r_{min} so that equation (2.13) which is derived from a Kerr metric, is still sufficiently precise. Furthermore, one would expect the DM halo to not extend to infinity, meaning that the DM density should also be zero outside of some large radius r_{max} with $r_{\text{max}} > r_{\text{min}}$, which will be kept as a free parameter in the calculations to study its effects. Taking these 'cut-off' radii into account, equation (3.18) takes the form

$$F(r) = \begin{cases} \exp\left\{-\frac{8\pi G}{c^2}\int_{r_{\text{min}}}^{r_{\text{max}}} r'\rho(r')\mathrm{d}r'\right\} & 0 < r \leq r_{\text{min}} \\ \exp\left\{-\frac{8\pi G}{c^2}\left[\frac{1}{r}\int_{r_{\text{min}}}^{r} r'^2\rho(r')\mathrm{d}r' + \int_{r}^{r_{\text{max}}} r'\rho(r')\mathrm{d}r'\right]\right\} & r_{\text{min}} < r \leq r_{\text{max}} \\ \exp\left\{-\frac{8\pi G}{c^2}\frac{1}{r}\int_{r_{\text{min}}}^{r_{\text{max}}} r'^2\rho(r')\mathrm{d}r'\right\} & r > r_{\text{max}} \end{cases} \tag{3.30}$$

and this is the expression for $F(r)$ that we will actually use in equation (3.27) for $f(r)$.

3.3 Equations of motion for photons

The shadow of a BH is determined by how photons move in its geometry. Since we assume that the only form of matter present is in the form of DM which does not interact with photons by definition, the photons may be treated as free particles. As discussed in section 2.3, the equations of motion for a free photon in a Hamiltonian framework are given by equations (2.12) under the condition (2.9). In this section, we will be guided by [47]. We use the metric (3.28) in order to study photons in the BH+DM system and write $(q, p) \equiv (t, r, \theta, \varphi, p_t, p_r, p_\theta, p_\varphi)$ for the phase space coordinates of some photon's trajectory. For simplicity, we will mostly drop the argument λ in our notation in this section. The first set of Hamilton equations (2.12) can then be written as

$$\dot{t} = -\frac{(r^2+a^2)^2 - a^2\Delta(r)\sin^2(\theta)}{\Sigma(r,\theta)\Delta(r)}p_t - \frac{a(r^2 - f(r)r^2)}{\Sigma(r,\theta)\Delta(r)}p_\varphi \quad , \tag{3.31}$$

$$\dot{r} = \frac{\Delta(r)}{\Sigma(r,\theta)}p_r \quad , \tag{3.32}$$

$$\dot{\theta} = \frac{1}{\Sigma(r,\theta)}p_\theta \quad , \tag{3.33}$$

$$\dot{\varphi} = -\frac{a(r^2 - f(r)r^2)}{\Sigma(r,\theta)\Delta(r)}p_t + \frac{a^2\cos^2(\theta) + r^2 f(r)}{\sin^2(\theta)\Sigma(r,\theta)\Delta(r)}p_\varphi \quad . \tag{3.34}$$

Some simplifications can be achieved by exploiting conserved quantities. Notice that since the metric components are independent of t and φ, it immediately follows from the second set of Hamilton equations that p_t and p_φ are both constant along a given geodesic. Let us denote these conserved quantities by $-E$ and L, respectively, and refer to E and L as the energy and the angular momentum of the photon. Another constant of motion was derived by Carter using Hamilton-Jacobi theory [51]. We use the letter $\mathcal{K}$ for what Carter labeled Q and refer to it as the Carter constant. It is given by

$$\begin{aligned}\mathcal{K} &= p_\theta^2 + \left(\frac{L^2}{\sin^2(\theta)} - a^2E^2\right)\cos^2(\theta) \\ &= \frac{1}{\Delta(r)}\Big[E(r^2+a^2) - aL\Big]^2 - \Delta(r)p_r^2 - (aE-L)^2\end{aligned} \tag{3.35}$$

in our notation. The equality can be verified using the null condition (2.9). If one knows the result already, it is easy to convince oneself that $\mathcal{K}$ is indeed constant along a geodesic by showing that the Poisson bracket of $\mathcal{K}$ with the Hamiltonian (2.11) vanishes.

Solving equation (3.35) for p_r and p_θ and substituting the results as well as $-E$ and L into the equations of motion (3.31) to (3.34), we find

$$\Sigma(r,\theta)\dot{t} = \frac{r^2+a^2}{\Delta(r)}\Big[E(r^2+a^2) - aL\Big] - a(aE\sin^2(\theta) - L) \quad , \tag{3.36}$$

$$\begin{aligned}\Sigma(r,\theta)\dot{r} &= \pm\sqrt{\left[E(r^2+a^2) - aL\right]^2 - \Delta(r)\left[(aE-L)^2 + \mathcal{K}\right]} \\ &=: \pm\sqrt{\mathcal{R}(r)} \quad ,\end{aligned} \tag{3.37}$$

$$\begin{aligned}\Sigma(r,\theta)\dot{\theta} &= \pm\sqrt{\mathcal{K} - \left(\frac{L^2}{\sin^2(\theta)} - a^2E^2\right)\cos^2(\theta)} \\ &=: \pm\sqrt{\Theta(\theta)} \quad ,\end{aligned} \tag{3.38}$$

$$\Sigma(r,\theta)\dot{\varphi} = \frac{a}{\Delta(r)}\Big[E(r^2+a^2) - aL\Big] - \left(aE - \frac{L}{\sin^2(\theta)}\right) \quad . \tag{3.39}$$

All of these equations need to be true in order to have a geodesic. However, the equations for $\dot{r}$ and $\dot{\theta}$ only depend on r and θ. When these two equations are solved, then the remaining two can in principle (and that is enough) also be solved by plugging in the solutions for $r(\lambda)$ and $\theta(\lambda)$. The only thing one needs to worry about is the existence of a solution to the r and θ equations which requires $\mathcal{R}(r(\lambda)) \geq 0$ and $\Theta(\theta(\lambda)) \geq 0$ for all λ. The first requirement is not a problem because for our purposes, as we will see in the next section, we are only interested in photons whose trajectories satisfy

$$\mathcal{R}(r(\lambda)) = 0 \quad , \tag{3.40}$$

$$\mathcal{R}'(r(\lambda)) = 0 \tag{3.41}$$

for all λ. The condition $\Theta(\theta(\lambda)) \geq 0$ is not met as easily, but we will implicitly take it into account in section 3.4 by restricting the range of the allowed radii r.

For later use, we will now find a connection between r and the conserved quantities E and L for trajectories for which (3.40) and (3.41) hold. Since $\mathcal{R}(r(\lambda)) = 0$ ensures that r is constant along the trajectory, we again abbreviate $r \equiv r(\lambda)$ to simplify the notation. From now on we assume $E(r) \neq 0$ and define $\xi(r) := L(r)/E(r)$ and $\eta(r) := \mathcal{K}(r)/(E(r)^2)$ where we emphasized in the notation that these quantities are conserved along a fixed trajectory, but may depend on the radius r of the orbit. The equations (3.40) and (3.41) can then be rewritten as

$$\left(r^2 + a^2 - a\xi(r)\right)^2 - \left[\eta(r) + (\xi(r) - a)^2\right]\left(r^2 f(r) + a^2\right) = 0 \quad , \tag{3.42}$$

$$4r\left(r^2 + a^2 - a\xi(r)\right) - \left[\eta(r) + (\xi(r) - a)^2\right]\left(2rf(r) + r^2 f'(r)\right) = 0 \tag{3.43}$$

which, for $a \neq 0$, can be solved for $\xi(r)$ and $\eta(r)$, resulting in

$$\xi(r) = \frac{(r^2 + a^2)(rf'(r) + 2f(r)) - 4(r^2 f(r) + a^2)}{a(rf'(r) + 2f(r))} \quad , \tag{3.44}$$

$$\eta(r) = \frac{r^3\left[8a^2 f'(r) - r(rf'(r) - 2f(r))^2\right]}{a^2(rf'(r) + 2f(r))^2} \quad . \tag{3.45}$$

3.4 Technical definition of a black hole shadow and Bardeen's coordinates

In order to find a more concrete definition of a BH shadow than in section 1.2, consider an observer who looks at a BH from far away in front of a star-lit background. Some photons that are emitted by the stars will approach the BH, be deflected and maybe even orbit around the BH several times but ultimately escape to infinity where they have a chance of being detected by the observer as a bright spot on the observer's sky. On the other hand, some photons will be emitted in a direction pointing close to the BH and will be captured by its gravitational field. Such photons cannot reach the observer. Even if we assume that there are light sources everywhere except between the observer and the BH, a part of the observer's sky will remain black if there does not exist any photon trajectory along the corresponding direction and which crosses the observer. This black patch is the BH shadow and it is fully determined if its boundary is known. The boundary points can be thought of as corresponding to those photons that neither move to infinity after passing the BH nor disappear behind the BH's event horizon. This limiting case consists of photons that orbit the BH indefinitely. Finding the BH shadow reduces to understanding what precisely these photon trajectories around the BH look like and how they translate to

points in the observer's sky. The first question has a quick answer: As it turns out, the BH shadow boundary can be found from photon orbits that satisfy the equations (3.40) and (3.41) [47, 52, 33]. For the second question, we need a mathematical prescription of how to map trajectories of photons that reach a distant observer onto a 2D plane. Phrased differently, we need a method to plot the BH shadow and this is achieved by introducing Bardeen's coordinates [53, 23].

In order to understand their meaning, consider the following: Assume an observer in 3D Euclidean space at a point P with cartesian coordinates (x_o, y_o, z_o) chosen in a way such that $y_o = 0$. We consider the plane through the origin and perpendicular to the line connecting the observer with the origin and call it the observer's sky. It consists of all points with cartesian coordinates (x, y, z) satisfying

$$x_o x + z_o z = 0 \quad . \tag{3.46}$$

The points with $(0, 1, 0)$ and $\left(-z_o/\sqrt{x_o^2 + z_o^2}, 0, x_o/\sqrt{x_o^2 + z_o^2}\right)$ as cartesian coordinates obviously lie in the observer's sky. Let e_x^O, e_y^O and e_z^O be the canonical cartesian unit vectors at the origin. Then the vectors $e_\alpha := e_y^O$ and $e_\beta := \frac{-z_o}{\sqrt{x_o^2+z_o^2}} e_x^O + \frac{x_0}{\sqrt{x_o^2+z_o^2}} e_z^O$ at the origin are orthogonal and have unit length as well and can be used to parametrize the observer's sky. The situation is visualized in figure 3.1.

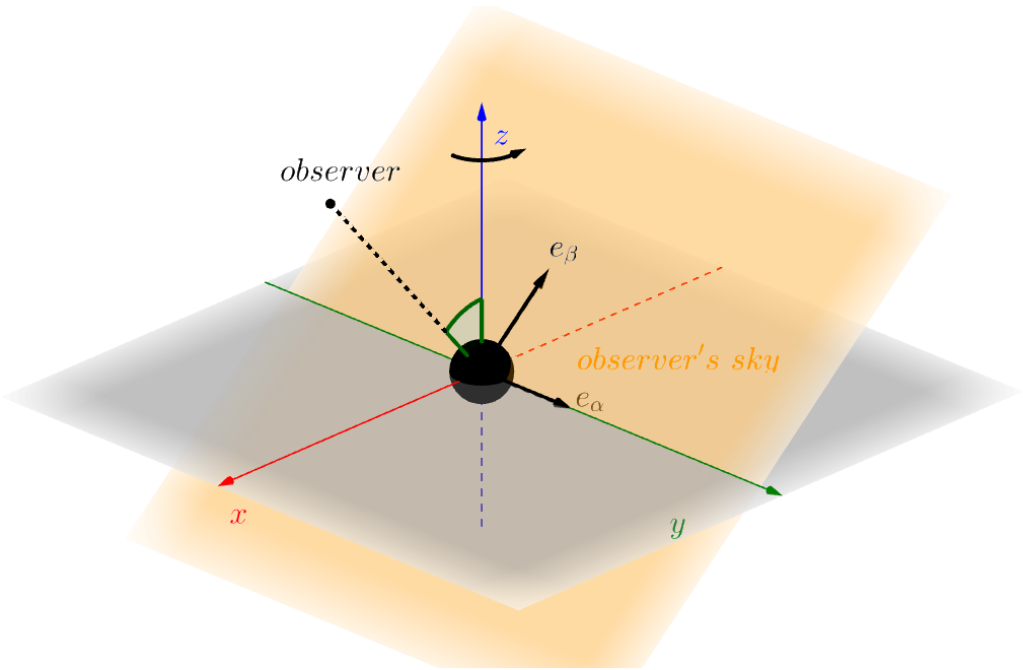

Figure 3.1: Overview of the geometry for the construction of Bardeen's coordinates. Created with GeoGebra.

Now consider a photon on a smooth trajectory $\lambda \mapsto \gamma(\lambda)$ with cartesian coordinates $(x(\lambda), y(\lambda), z(\lambda))$ crossing the observer. Then there exists a λ_o such that $\gamma(\lambda_o) = P$. The tangent vector v to γ at P is given by $v = \dot{x}(\lambda_o)e_x^P + \dot{y}(\lambda_o)e_y^P + \dot{z}(\lambda_o)e_z^P$ with the parallel-transported canonical unit vectors e_x^P, e_y^P and e_z^P at P (this is well-defined because of the flatness of Euclidean space). Construct a line l whose cartesian coordinates are parametrized by $\mu \mapsto (x_o, 0, z_o) + \mu(\dot{x}(\lambda_o), \dot{y}(\lambda_o), \dot{z}(\lambda_o))$. This line obviously meets the observer and its tangent vector at P is equal to v and can thus be interpreted as the direction from which the observer would see the approaching photon. The point in the observer's sky that is assigned to this photon is defined to be the unique point Q where the line l intersects the observer's sky. Using equation (3.46) it can be shown that Q is given by

$$Q \mathrel{\widehat{=}} \mu\dot{y}(\lambda_o)(0,1,0) + \frac{\sqrt{x_o^2+z_o^2}}{x_o}\left(z_o + \mu\dot{z}(\lambda_o)\right)\left(\frac{-z_o}{\sqrt{x_o^2+z_o^2}}, 0, \frac{x_o}{\sqrt{x_o^2+z_o^2}}\right) \quad \text{in cartesian coordinates} \tag{3.47}$$

with $\mu = -\frac{x_o^2+z_o^2}{x_o\dot{x}(\lambda_o)+z_o\dot{z}(\lambda_o)}$. From this representation one can simply read off the α-β coordinates as the coefficients of the expansion. Changing from cartesian to spherical coordinates (r, θ, φ) finally results in

$$Q \mathrel{\widehat{=}} \left(-r_o^2 \sin(\theta_o)\frac{\dot{\varphi}(\lambda_o)}{\dot{r}(\lambda_o)}, r_o^2\frac{\dot{\theta}(\lambda_o)}{\dot{r}(\lambda_o)}\right) \quad \text{in } \alpha\text{-}\beta \text{ coordinates.} \tag{3.48}$$

In order to transfer this into the GR setting that the BH shadow calculations are based on, we identify the spherical coordinates (r, θ, φ) in equation (3.48) with the spatial coordinates that the metric (3.28) is written in and place the singularity of the BH in the origin. Since the calculations above made use of the flatness of Euclidean space, it is best to only accept equation (3.48) in the limit as $r_o \to \infty$, i.e. with an observer 'at infinity', where spacetime can be approximated as flat:

$$\alpha := \lim_{r_o\to\infty}\left(-r_o^2 \sin(\theta_o)\frac{\dot{\varphi}(\lambda_o)}{\dot{r}(\lambda_o)}\right) \quad , \tag{3.49}$$

$$\beta := \lim_{r_o\to\infty}\left(r_o^2\frac{\dot{\theta}(\lambda_o)}{\dot{r}(\lambda_o)}\right) \tag{3.50}$$

These or very similar expressions for Bardeen's α-β coordinates appear in other publications, e.g. in [54] and [47].

We will evaluate (3.49) and (3.50) with the equations of motion (3.37), (3.38) and

(3.39) for photons. We remember that $\lim_{r_o \to \infty} f(r_o) = 1$ and arrive at

$$\alpha(r) = -\frac{\xi(r)}{\sin(\theta_o)} \quad , \tag{3.51}$$

$$\beta_\pm(r) = \pm\sqrt{\eta(r) + a^2\cos^2(\theta_o) - \xi(r)^2\cot^2(\theta_o)} \quad . \tag{3.52}$$

with $\xi(r)$ and $\eta(r)$ as in (3.44) and (3.45) because we are looking Bardeen's coordinates for the BH shadow boundary points. In this step the $+$ sign needs to be chosen for equation (3.37) because we want to consider photons approaching the observer at infinity and those have $\dot{r}(\lambda_o) > 0$. For $\dot{\theta}$, the ambiguity in sign cannot be resolved. The BH shadow boundary in Bardeen's coordinates is then obtained by plotting the images of the parametric curves $r \mapsto (\alpha(r), \beta_+(r))$ and $r \mapsto (\alpha(r), \beta_-(r))$. Figure 3.2 shows a helpful visualization of this concept.

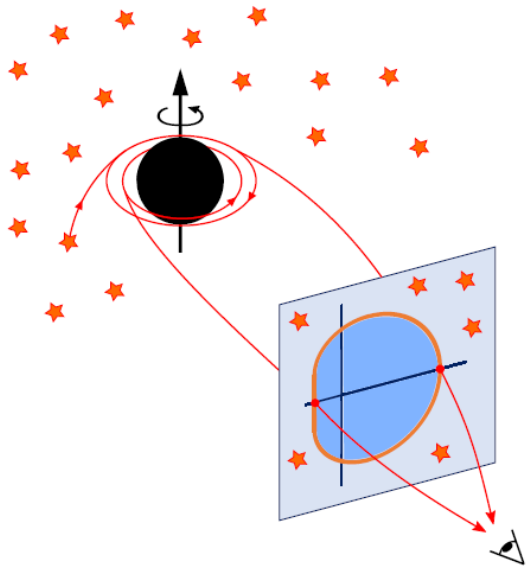

Figure 3.2: Illustration showing how a BH shadow boundary in Bardeen's coordinates is generated. Adapted from [23].

It is useful to plot α values on the horizontal and β values on the vertical axis because, by construction, α has the meaning of the width of the BH shadow perpendicular to the axis of symmetry of the system while β measures the BH shadow's size parallel to the axis of symmetry, both with respect to an observer at infinity. This interpretation is supported by equation (3.51) because α is proportional to the angular momentum L.
As a consequence of the above, the BH shadow is symmetric with respect to reflection about the α-axis. From the equations (3.51) and (3.52) it is also apparent that the coordinates α and $\beta_\pm$ do not change when replacing θ_o by $\pi - \theta_o$ which means that the upper and the lower hemispheres are in that sense on equal footing. This was to be expected from the axial symmetry of the spacetime at hand

and is therefore a good cross-check.

Unfortunately, the calculation of a BH shadow becomes a little more complicated because there are some restrictions we need to impose on the range of allowed r values. Firstly, the obvious requirement

$$\eta(r) + a^2 \cos^2(\theta_o) - \xi(r)^2 \cot^2(\theta_o) \geq 0 \tag{3.53}$$

guarantees that $\beta_\pm$ can be calculated in the first place. Secondly, remember that we want to consider closed photon orbits as the limiting case between photons reaching the observer and photons ultimately falling into the BH. However, if r is inside the radius r_{oeh} of the BH's outermost event horizon, it is impossible for photons at a radius that is only slightly larger than r to escape to infinity. For the construction of the BH shadow, we take this into account by further requiring

$$r > r_{\text{oeh}} \quad . \tag{3.54}$$

In analogy to how the outer event horizon of a Kerr BH is found, r_{oeh} is given by the largest solution to $\Delta(r) = 0$ [11] where $\Delta(r) = r^2 f(r) + a^2$ as in equation (3.28). For details on the existence and uniqueness of r_{oeh} in our situation, see A.1.

As a concluding note, the geometric approach to Bardeen's coordinates that we presented here hides something very subtle: Their construction assumes that a photon actually reaches the observer. However, for the calculation of the BH shadow boundary we use photon orbits that never reach the observer, but we still assign Bardeen's coordinates to them as if they did. For a short discussion of this issue we refer to the paragraph "Injection of Light Rays into a Photon Orbits [sic]" in the appendix of [52].

3.5 Performing the black hole shadow calculations

The results for the BH shadow boundaries in section 4.2 are obtained by running a combination of Python codes. These were mainly written by myself. The code which calculates the DM densities was written by Lukas Hölker for the most part [39] with a couple of adaptations from my side. Credits also go to Jorden Roberts for creating a very reliable root-finding algorithm and for his Mathematica calculations of r_{min} as well as to Niklas Becker for rewriting parts of my code to increase its speed. Apart from the Mathematica code, all the necessary files can be found on my GitHub repository [55].

The computations take the following pieces of data as variable input: M_{BH}, ρ_0, r_0, a, r_{max} and θ_o and are carried out in the following way:

1. The ten DM density functions each for Sgr A* and M87* are determined as described in section 3.1. This step makes use of the specific values of M_{BH}, ρ_0 and r_0. For reference, we also include the vacuum case where the DM vanishes everywhere.

2. For all BHs, DM density profiles and spin parameters a, r_{min} is found with Jorden Roberts' code.

3. Together with r_{min} and r_{max}, the DM densities are used to calculate $f(r)$ with the equations (3.27) and (3.30) as well as the derivative $f'(r)$.

4. We find the outermost event horizon r_{oeh} as the largest root of Δ with $\Delta(r) = r^2 f(r) + a^2$ as in (3.28).

5. For any $r > r_{\mathrm{oeh}}$, we need to calculate $\xi(r)$ and $\eta(r)$ using equations (3.44) and (3.45) and check if condition (3.53) is satisfied with the chosen θ_o. If it is, save the pair $(\alpha(r), \beta_+(r))$ with $\alpha(r)$ and $\beta_+(r)$ given by (3.51) and (3.52).

6. By plotting the points $(\alpha(r), \beta_+(r))$ and $(\alpha(r), \beta_-(r)) = (\alpha(r), -\beta_+(r))$ for all such r, the BH shadow boundary is drawn.

7. For some BH shadow plots, the ranges of both axes are set manually to zoom into parts of the BH shadow boundaries that are of particular interest.

4 Results

4.1 Densities of the dark matter halos

The numerical results for the densities of the different DM halos are presented in figure 4.1 and table 4.1. One has to keep in mind that the units in the DM density plots are different between Sgr A* and M87* because they depend on the masses of the BHs. In units independent of M_{BH}, the following observations might not necessarily be true. However, it makes sense to work in units of GM_{BH}/c^2 nonetheless because many essential geometric quantities like the Schwarzschild radius scale with the BH mass.

An immediate observation is that the overall shapes of the curves are very similar and that for both BHs, the DM densities at small r have the same ordering: The spiked NFW model leads to the largest densities, followed by the spiked SIDM models and the NFW profile without a spike. By far the smallest densities near the BH are obtained by the spike-less SIDM profiles. It is remarkable that, near the BH, some density profiles differ by several orders of magnitude from other profiles. This is especially true when one compares a profile with a spike with its counterpart without one. The strong increase in density after adding a spike confirms the mathematical observation $\gamma \geq \Gamma$ from section 2.1.3.
Clearly visible are the different slopes of the density profiles at small radii: Within a spike, the density $\rho(r)$ depends on r like $\rho(r) \sim r^{-\gamma}$ which translates into a straight line in a double-logarithmic plot. Since the spike is the steepest for the spiked NFW model ($\gamma = 7/3$), its density approaches those of the spiked SIDM profiles ($\gamma = 7/4$) with increasing r. All spiked SIDM profiles share $\gamma = 7/4$ which leads to their lines being parallel in the plots. The NFW profile also seems to have a purely exponential shape with $\rho(r) \sim r^{-1}$ at small r. This is due to the behavior $\rho_{\mathrm{NFW}}(r) \sim r^{-1}$ for $r \ll r_0$ that we already saw in section 2.1.1. The SIDM profiles without spikes are all close to constant over a large distance. This meets the expectations because the model is already known to form cored density profiles, recall the discussion in section 2.1.2.
Within the groups of SIDM and spiked SIDM profiles, a smaller self-interaction cross section leads to a higher density, although the differences are rather small compared to how far the NFW and spiked NFW profiles deviate from the SIDM and spiked SIDM profiles in general. A smaller cross section shifts the matching radius r_{m} to smaller radii for the reason that r_{m} was defined to be the radius where only one self-interaction is expected during a time span of t_{age} and the decrease in cross section needs to be compensated by an increase in DM density. One can imagine that the matching radius becomes even smaller for $\sigma/m \to 0^+$

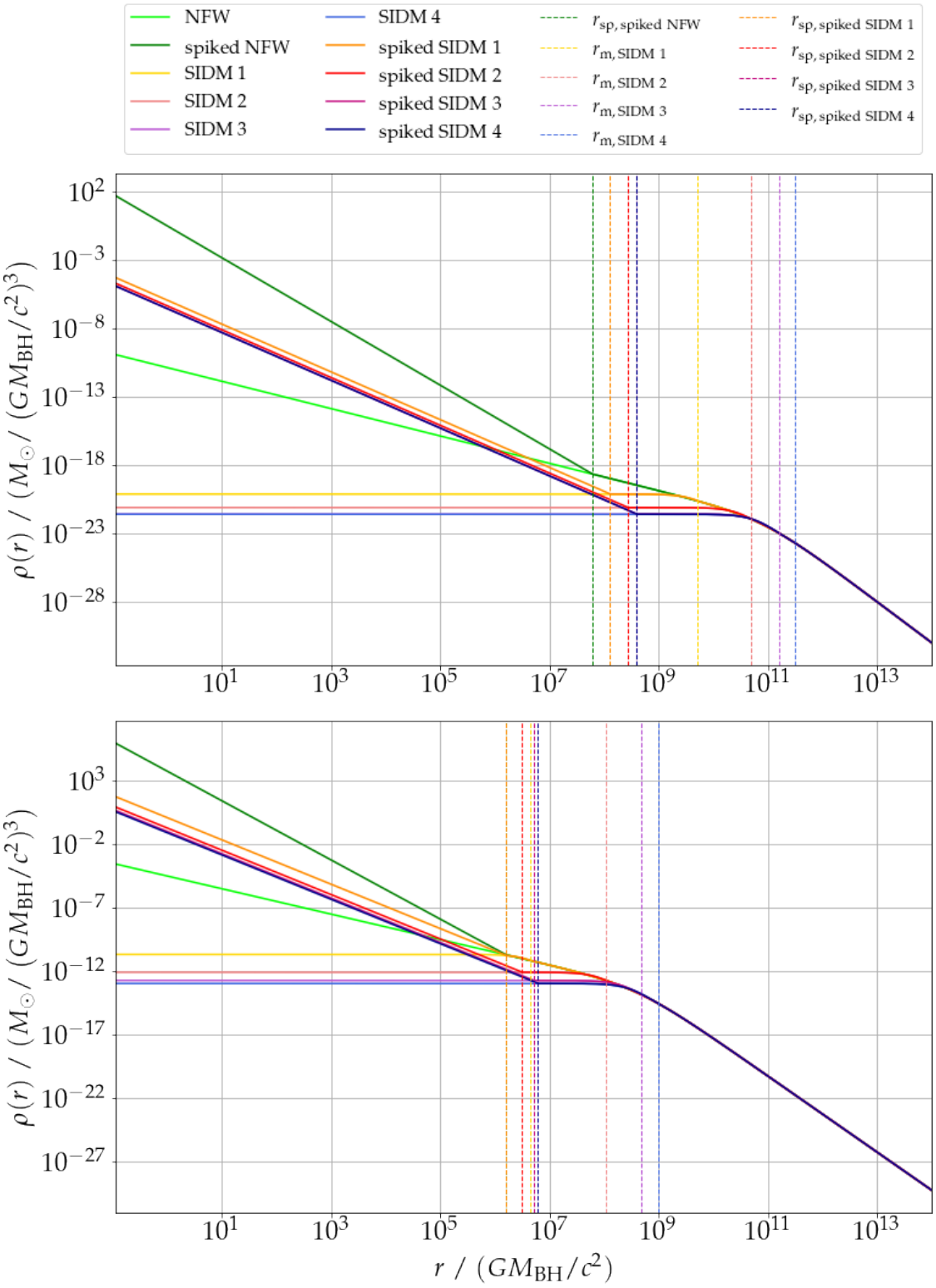

Figure 4.1: DM densities around Sgr A* (top) and M87* (bottom) for the ten different DM halo models. The dashed lines mark the matching and spike radii. Note that the cut-off outside of $[r_{\mathrm{min}}, r_{\mathrm{max}}]$ is not considered here because r_{min} and r_{max} are not fixed by the BH and the DM model.

	$r_{\mathrm{sp}}/(GM_{\mathrm{BH}}/c^2)$	$r_{\mathrm{m}}/(GM_{\mathrm{BH}}/c^2)$
NFW	-	-
spiked NFW	$5.97 \cdot 10^7$	-
SIDM 1	-	$5.20 \cdot 10^9$
SIDM 2	-	$4.85 \cdot 10^{10}$
SIDM 3	-	$1.59 \cdot 10^{11}$
SIDM 4	-	$3.08 \cdot 10^{11}$
spiked SIDM 1	$1.28 \cdot 10^8$	$5.20 \cdot 10^9$
spiked SIDM 2	$2.70 \cdot 10^8$	$4.85 \cdot 10^{10}$
spiked SIDM 3	$3.90 \cdot 10^8$	$1.59 \cdot 10^{11}$
spiked SIDM 4	$3.93 \cdot 10^8$	$3.08 \cdot 10^{11}$

	$r_{\mathrm{sp}}/(GM_{\mathrm{BH}}/c^2)$	$r_{\mathrm{m}}/(GM_{\mathrm{BH}}/c^2)$
NFW	-	-
spiked NFW	$1.57 \cdot 10^6$	-
SIDM 1	-	$4.39 \cdot 10^6$
SIDM 2	-	$1.09 \cdot 10^8$
SIDM 3	-	$4.80 \cdot 10^8$
SIDM 4	-	$9.88 \cdot 10^8$
spiked SIDM 1	$1.60 \cdot 10^6$	$4.39 \cdot 10^6$
spiked SIDM 2	$3.12 \cdot 10^6$	$1.09 \cdot 10^8$
spiked SIDM 3	$5.09 \cdot 10^6$	$4.80 \cdot 10^8$
spiked SIDM 4	$6.10 \cdot 10^6$	$9.88 \cdot 10^8$

Table 4.1: Spike and matching radii for the different DM models in the Sgr A* (top) and M87* (bottom) systems.

so that the part of an SIDM profile that is equal to an NFW profile by construction becomes larger and larger. In the limit, this makes the SIDM profile converge to the NFW profile as it needs to.
The most interesting observations can be made between the regions of the different spike radii and about three orders of magnitude of r within. Due to the different slopes, the spiked SIDM densities are eventually 'overtaken' by the NFW density and this ordering remains true until very far out where they approach each other again. At the spike radii, the corresponding profiles with and without spikes become identical, so any difference that we are going to see between their BH shadows must be a consequence of the difference in density within the spike radii. An analogous statement can be made for the matching radii: Outside its matching radius, a particular density profile is identical to the NFW profile and anything distinguishing the BH shadows of those two systems

is necessarily an effect of the different densities inside the matching radius. One might think that the spike and matching radii are so far away from the BHs that the densities in those regions should not affect the BH shadows. This point will be addressed in section 4.2.

All observations so far are true both for Sgr A* and M87*. However, there are a couple of differences in the density profiles between these two systems. In general, the DM densities are larger around M87*, but around Sgr A* they cover a larger range. If one considers the densities close to the BHs, for example at $r = 10\,GM_{\mathrm{BH}}/c^2$, one notices that the DM densities for Sgr A* vary over about 18 orders of magnitude, while it is roughly 14 for M87*. It is also clearly visible that the spike and matching radii are located at larger distances in the Sgr A* system. Therefore, the density profiles maintain their shapes until these large radii. For M87*, the smaller spike and matching radii have the consequence that the densities are equal over a much larger interval in r. This is a good reason to suspect that the outer parts ($\gtrsim 10^9\,GM_{\mathrm{BH}}/c^2$) of the halos should not matter for the relative sizes of the M87* shadows, but for Sgr A*, they might. For M87*, the matching radius for the (spiked) SIDM 1 profiles lies between the different spike radii, in contrast to the situation for Sgr A* where the spike and matching radii are clearly separated from each other. Therefore we might expect the (spiked) SIDM 1 profiles to behave differently between the two systems.

4.2 Properties of the black hole shadows

In this section we will describe and analyze the results for the BH shadows of Sgr A* and M87* under a couple of different conditions. This will also allow us to see if the expectations from section 4.1 are actually fulfilled.
Firstly, we will explore the effects of a varying spin parameter a and inclination angle θ_o of the observer while we keep the other parameters constant. It turns out that all effects are qualitatively equal for the Sgr A* and M87* shadows, so for simplicity we will only look at M87*. Furthermore, we will fix $r_{\mathrm{max}} = 10^{14}\,GM_{\mathrm{BH}}/c^2$ for the moment. This value has not been chosen for physical reasons, but simply because it is close to the largest one that our code can handle. However, even larger r_{max} are not sensible, at least for the M87* system, because in this case $10^{14}\,GM_{\mathrm{BH}}/c^2 \approx 30\,\mathrm{Gpc}$ which is larger than the estimated radius of the observable universe [56]. In addition, as apparent from figure 4.1, the DM densities would be the same and extremely low for $r > 10^{14}\,GM_{\mathrm{BH}}/c^2$, so this choice of r_{max} will not affect the following results in any noticeable way.
The three figures 4.2, 4.3 and 4.4 show the results for the BH shadows of M87* as they depend on a and θ_o.

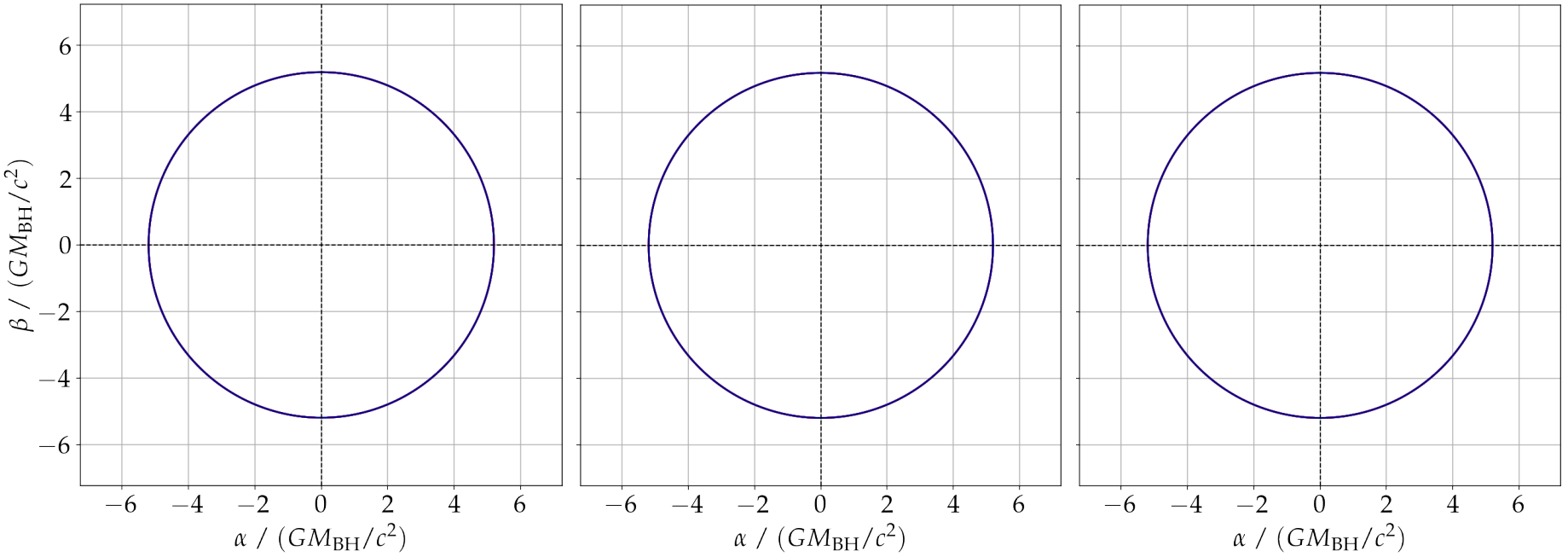

Figure 4.2: Shadows of M87* with fixed $a = 0.001\, GM_{\mathrm{BH}}/c^2$ and $\theta_o = \pi/16$, $\pi/4$ and $\pi/2$ from left to right. The shadows for all different DM models are plotted, but due to their strong similarities only the one that was plotted last, namely for spiked SIDM 4, is visible in each plot. This is why we left out the legend for the different DM models.

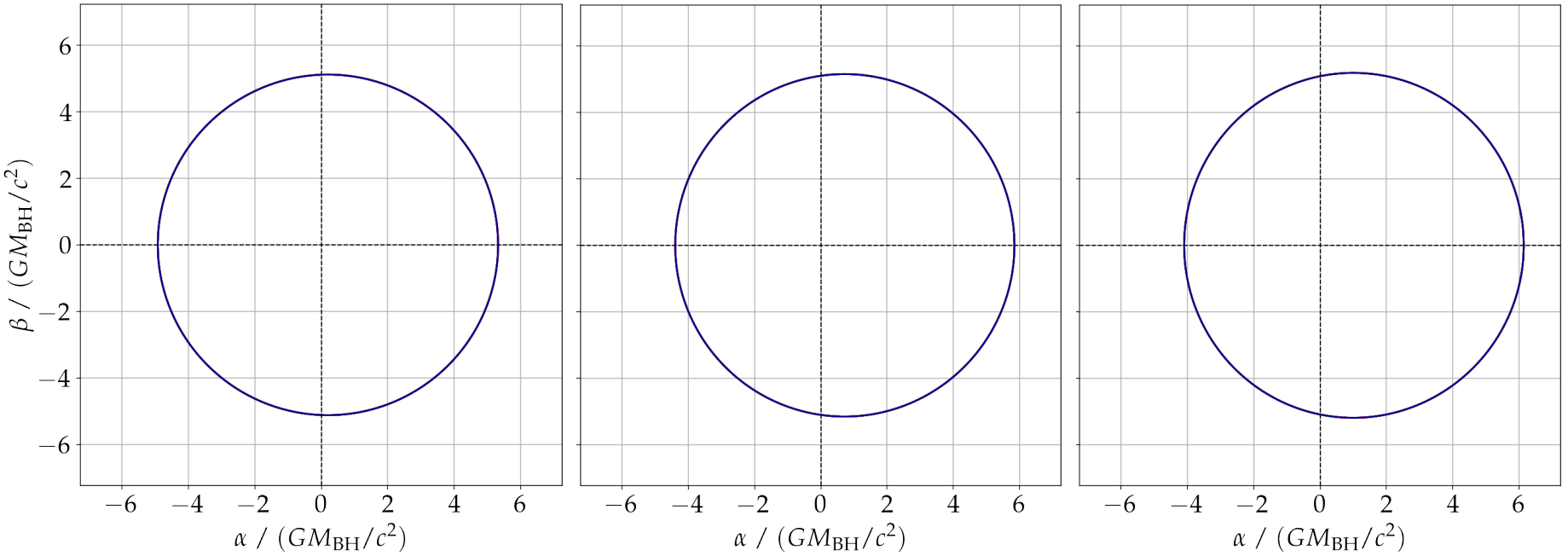

Figure 4.3: Shadows of M87* with fixed $a = 0.5\,GM_{\mathrm{BH}}/c^2$ and $\theta_o = \pi/16$, $\pi/4$ and $\pi/2$ from left to right. Please note the additional remark in the caption of figure 4.2.

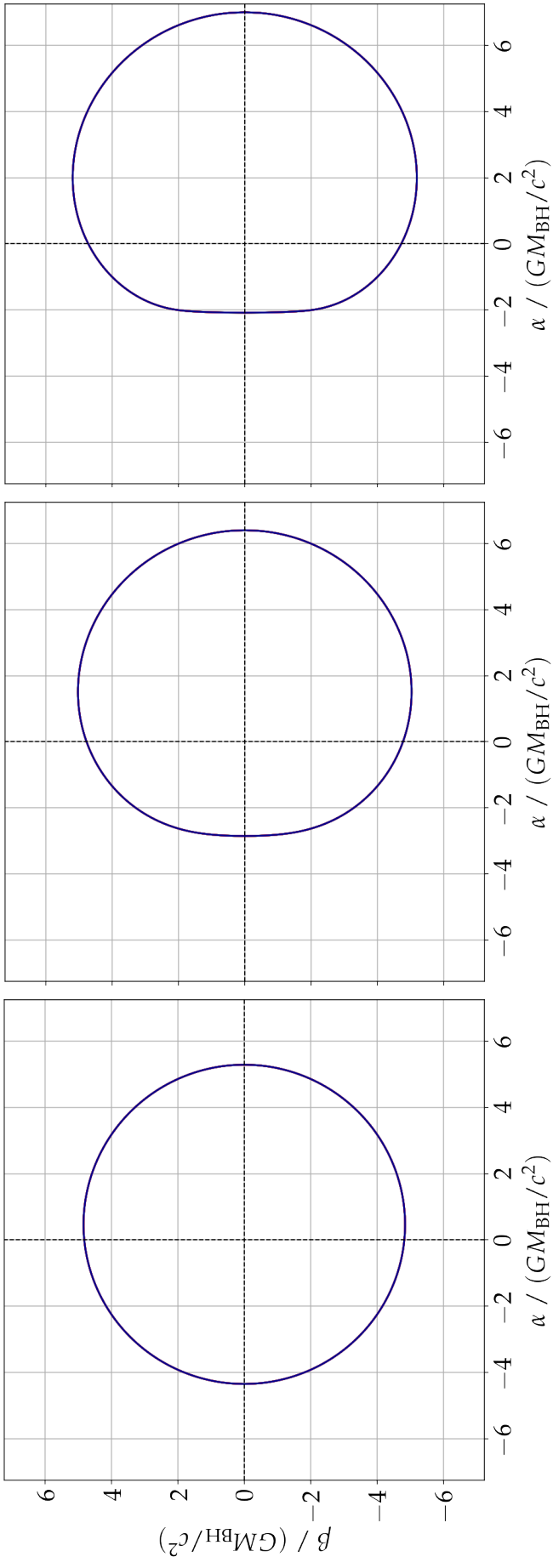

Figure 4.4: Shadows of M87* with fixed $a = 0.999\,GM_{\mathrm{BH}}/c^2$ and $\theta_o = \pi/16$, $\pi/4$ and $\pi/2$ from left to right. The remark in the caption of figure 4.2 also applies here.

First of all, it might come as a surprise that only the shadows using the spiked SIDM 4 model are visible. This is not a mistake, but due to the fact that the different DM models lead to BH shadows that are extremely similar in size and shape. With the axes on this scale, the BH shadows within one plot are basically identical and hence only the one that was plotted last is visible. We will take a closer look and zoom into the BH shadows later in this section to see the actual differences.
Comparing the different plots in the figures 4.2, 4.3 and 4.4, one realizes that the BH shadows are almost circular and centered for small a, independent of θ_o. This meets the expectations because in the limit $a \to 0$, spacetime recovers its spherical symmetry and no observer position is preferred. On the contrary, for the two larger values of a, the effects of θ_o become apparent: The more the observer approaches $\theta_o = \pi/2$, i.e. the equatorial plane, the stronger the BH shadows are deformed and shifted into the positive α-direction. In the most extreme case with $a = 0.999\, GM_{\mathrm{BH}}/c^2$ and $\theta_o = \pi/2$, the left-most points of the BH shadows basically form a straight line while the right halves of the shadows preserve their overall shapes.
One can understand these properties by recalling figure 2.2. Photons contributing to the left rims of the BH shadow boundaries move on prograde orbits in or close to the equatorial plane. Since circular photon orbits exist at smaller radii if the photon is in prograde rather than retrograde motion with the BH, the BH shadows get a 'dent' on their very left. Analogously, retrograde photon orbits that are responsible for the right-most points of the BH shadow boundaries are shifted to larger radii with increasing a, moving these points in the plots to the right as well. That this shift of points to the right is stronger at negative rather than positive α is due to the fact that $r_{\text{massless, prograde}}$ depends more strongly on a than $r_{\text{massless, retrograde}}$, see figure 2.2 again. The effect of θ_o on the BH shadows is also clear: At small θ_o, the observer's line of sight almost coincides with the BH's axis of symmetry so that, again, no direction in the observer's sky is preferred and this is true for all a. With increasing θ_o up to $\pi/2$, the observer's line of sight deviates more strongly from the axis of symmetry and the prograde and retrograde photon orbits start to show their effects as discussed before.

Secondly, we are going to examine the relative sizes of the BH shadows as they depend on the upper cut-off radius $r_{\max}$. We will restrict ourselves to the case $a = 0.5\, GM_{\mathrm{BH}}/c^2$ and $\theta_o = \pi/4$. For the standard value $r_{\max} = 10^{14}\, GM_{\mathrm{BH}}/c^2$, consider the figures 4.5 and 4.6. They show the shadows of Sgr A* and M87* within the DM halos again, but now at different levels of magnification to be able to tell them apart. The zooms are centered at the arbitrarily chosen value $\alpha = 4.5\, GM_{\mathrm{BH}}/c^2$ and the α and β axes are equally scaled within one plot.

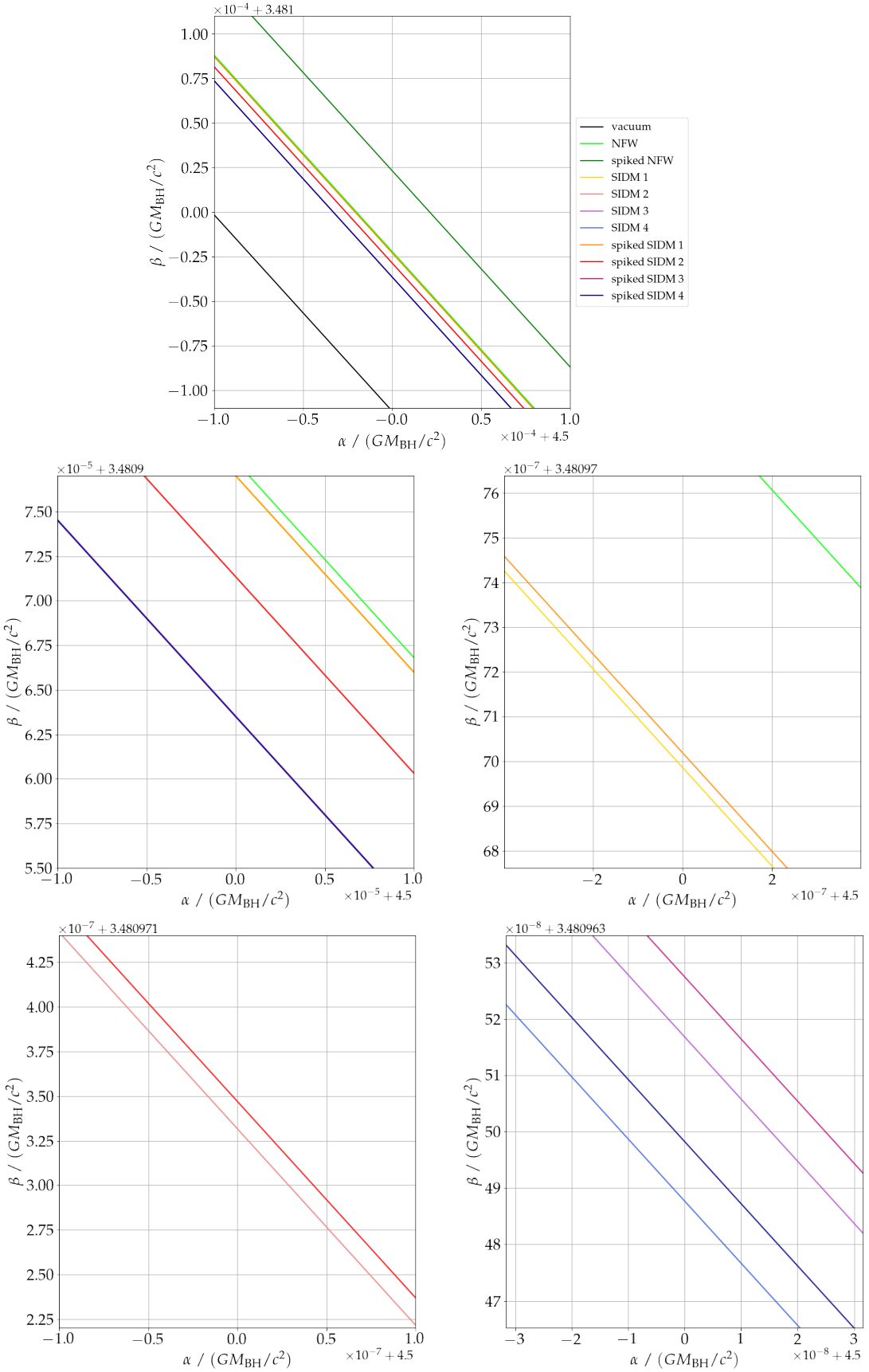

Figure 4.5: Shadow boundaries of Sgr A* with $a = 0.5\,GM_{\rm BH}/c^2$, $\theta_o = \pi/4$ and $r_{\rm max} = 10^{14}\,GM_{\rm BH}/c^2$ at different zooms around $\alpha = 4.5\,GM_{\rm BH}/c^2$.

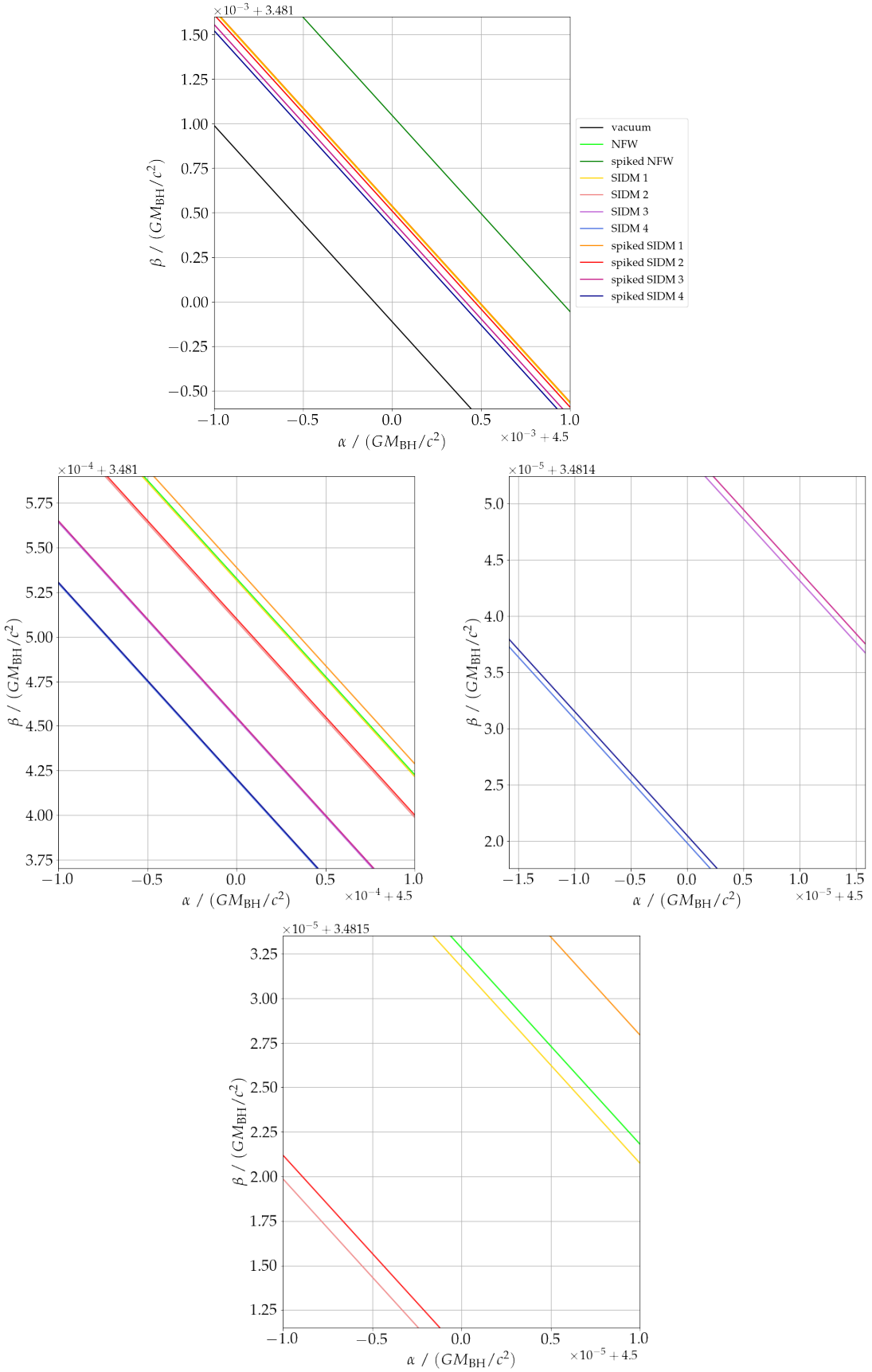

Figure 4.6: Shadow boundaries of M87* with $a = 0.5\,GM_{\rm BH}/c^2$, $\theta_o = \pi/4$ and $r_{\rm max} = 10^{14}\,GM_{\rm BH}/c^2$ at different zooms around $\alpha = 4.5\,GM_{\rm BH}/c^2$.

We see immediately that we need a precision of around 10^{-3} to $10^{-4}\, GM_{\mathrm{BH}}/c^2$ to see the lines for the vacuum and the spiked NFW profiles separate clearly from the rest. With this knowledge, it is not surprising that there appeared to only be a single line in the plots showing the full BH shadows. The spiked NFW profile leads to the largest and the vacuum to the smallest BH shadows. It is intuitively clear that a larger DM density increases the gravitational pull towards the BH and therefore forces circular photon orbits to larger radii. This effect leads to larger BH shadows. How precisely the size of a BH shadow depends on the density of the surrounding DM halo will be studied in section 4.3.
In order to resolve the remaining nine BH shadows, we increase the magnification. In the case of Sgr A*, we need to zoom to the length scale $10^{-8}\, GM_{\mathrm{BH}}/c^2$ before can read off the relative sizes of the different BH shadows. For Sgr A*, the BH shadow corresponding to the NFW profile is the second largest. The lines for the eight spiked and non-spiked SIDM profiles form four pairs that are mostly isolated from each other. Only the lines for the (spiked) SIDM 3 and (spiked) SIDM 4 BH shadows are relatively close together. The BH shadows decrease in size if the DM particles' self-interaction cross section increases. This is because a higher probability for scattering leads to a lower DM density, as previously discussed in section 4.1. For a fixed cross section, the spiked SIDM model exhibits a larger density than its counterpart without a spike and this is also reflected in the sizes of the BH shadows: Those for a spiked profile are larger although the effect of the spike is rather weak, especially for the higher cross sections (notice the different scales of the plots). For very low cross sections, the spike is more dominant and one can easily imagine that, in the limit $\sigma/m \to 0^+$, the BH shadows for the (spiked) SIDM models converge to those of the (spiked) NFW models. This actually has to be the case because a cross section of zero reduces the (spiked) SIDM profile to a (spiked) NFW density profile. In short, we can conclude that the self-interaction cross section is more important to the BH shadow size than the existence of a density spike.
Almost exactly the same observations are also true when one studies the shadows of M87*. The only notable difference is that the spiked SIDM 1 and the NFW models switch positions in terms of their BH shadow sizes. We can understand this by comparing the corresponding density profiles between Sgr A* and M87*. In the Sgr A* system, the NFW density eventually becomes larger than that of spiked SIDM 1 which does not seem to be the case for M87* or only in a very small interval.

We can repeat a similar analysis for smaller r_{max} and arrive at the results in table 4.2. DM following a spiked NFW profile is by far the most dense in our calculations, so it is clear that the BH shadows are also the largest in the spiked NFW

10^4	10^6	10^8	10^{10}	10^{12}	10^{14}
sp. NFW	sp. NFW	sp. NFW	sp. NFW	sp. NFW	sp. NFW
sp. SIDM 1	sp. SIDM 1	NFW	NFW	NFW	NFW
sp. SIDM 2	sp. SIDM 2	sp. SIDM 1	sp. SIDM 1	sp. SIDM 1	sp. SIDM 1
sp. SIDM 3	sp. SIDM 3	sp. SIDM 2	SIDM 1	SIDM 1	SIDM 1
sp. SIDM 4	sp. SIDM 4	sp. SIDM 3	sp. SIDM 2	sp. SIDM 2	sp. SIDM 2
NFW	NFW	sp. SIDM 4	SIDM 2	SIDM 2	SIDM 2
SIDM 1	SIDM 1	SIDM 1	sp. SIDM 3	sp. SIDM 3	sp. SIDM 3
SIDM 2	SIDM 2	SIDM 2	SIDM 3	SIDM 3	SIDM 3
SIDM 3	SIDM 3	SIDM 3	sp. SIDM 4	sp. SIDM 4	sp. SIDM 4
SIDM 4	SIDM 4	SIDM 4	SIDM 4	SIDM 4	SIDM 4
vacuum	vacuum	vacuum	vacuum	vacuum	vacuum

10^4	10^6	10^8	10^{10}	10^{12}	10^{14}
sp. NFW	sp. NFW	sp. NFW	sp. NFW	sp. NFW	sp. NFW
sp. SIDM 1	sp. SIDM 1	sp. SIDM 1	sp. SIDM 1	sp. SIDM 1	sp. SIDM 1
sp. SIDM2	NFW	NFW	NFW	NFW	NFW
sp. SIDM 3	sp. SIDM 2	SIDM 1	SIDM 1	SIDM 1	SIDM 1
sp. SIDM 4	sp. SIDM 3	sp. SIDM 2	sp. SIDM 2	sp. SIDM 2	sp. SIDM 2
NFW	SIDM 1	SIDM 2	SIDM 2	SIDM 2	SIDM 2
SIDM 1	sp. SIDM 4	sp. SIDM 3	sp. SIDM 3	sp. SIDM 3	sp. SIDM 3
SIDM 2	SIDM 2	SIDM 3	SIDM 3	SIDM 3	SIDM 3
SIDM 3	SIDM 3	sp. SIDM 4	sp. SIDM 4	sp. SIDM 4	sp. SIDM 4
SIDM 4	SIDM 4	SIDM 4	SIDM 4	SIDM 4	SIDM 4
vacuum	vacuum	vacuum	vacuum	vacuum	vacuum

Table 4.2: Ranking of BH shadow sizes for Sgr A* (top) and M87* (bottom) around $\alpha = 4.5\,GM_{\rm BH}/c^2$ with $a = 0.5\,GM_{\rm BH}/c^2$, $\theta_o = \pi/4$ for different $r_{\rm max}$. The head of each column is the respective value of $r_{\rm max}$ in units of $GM_{\rm BH}/c^2$. Within a column, the sizes of the BH shadows decrease from top to bottom. A colored entry indicates that the BH shadow could not be distinguished from the rest, even at a precision of about $10^{-13}\,GM_{\rm BH}/c^2$, and its position in the column was guessed based on our expectations. "sp." is short for "spiked".

model. This is true for all r_{max} and both Sgr A* and M87*. On the opposite end of the list, we find the vacuum case as it must be. The SIDM 4 model always takes the second-to-last place. The other DM models show a more interesting behavior, but let us first note the following: It turns out that the Sgr A* shadows for an SIDM halo and for the vacuum are extremely similar if $r_{\text{max}} = 10^4\, GM_{\text{BH}}/c^2$ or $10^6\, GM_{\text{BH}}/c^2$. In fact, they are so similar that we cannot distinguish them at all with our methods. This is most likely a consequence of the four SIDM densities being of the order of about $10^{-20}\, M_\odot (GM_{\text{BH}}/c^2)^{-3}$ up until $r = 10^9\, GM_{\text{BH}}/c^2$. Because of this, the densities are not only very small in total, making the BH shadows indistinguishable from that of Sgr A* in vacuum, but also too similar relative to each other so that we cannot differentiate the BH shadows for the different cross sections. The reason that this does not happen in the M87* system is that the SIDM densities are much larger (in the BH-dependent units) to begin with.

Apart from that, at small r_{max}, the spiked SIDM models are grouped together, separated from their equivalent models without a spike. It would be surprising if this were not the case because within comparatively small radii a spike adds several orders of magnitude to the density. The density of the NFW profile is between the SIDM and the spiked SIDM ones and the same is true for the BH shadow sizes. As observed earlier for $r_{\text{max}} = 10^{14}\, GM_{\text{BH}}/c^2$, the BH shadows always grow when the cross section is reduced, independent of the maximal radius of the DM halo. The contribution of the spike, on the other hand, depends on r_{max}: The larger the halo becomes, the smaller the fraction that is described by the spike gets and the shape of the density profile very far away from the BH becomes more important. This causes the initial splitting between the groups of spiked SIDM and SIDM models to disappear. Instead, these models increasingly pair up according to their cross sections. For Sgr A*, the relative sizes of all BH shadows stabilize when r_{max} reaches and exceeds $10^{10}\, GM_{\text{BH}}/c^2$ whereas this already happens at $10^8\, GM_{\text{BH}}/c^2$ for M87*. Once again, this can easily be explained by the densities. Since the spike and matching radii are smaller in the M87* system, the densities equalize closer to the BH. Finally, we see the different ordering of the NFW and the spiked SIDM 1 models in tables for Sgr A* and M87* at intermediate and large r_{max}, so the observation made in figures 4.5 and 4.6 was not exclusive to $r_{\text{max}} = 10^{14}\, GM_{\text{BH}}/c^2$.

In summary, the results in table 4.2 are physically plausible and it is not difficult to see the correspondence between the DM densities and the BH shadow sizes. Note that the discussion in this section assumed $a = 0.5\, GM_{\text{BH}}/c^2$, $\theta_o = \pi/4$ and that it was based only on the arbitrarily chosen region around $\alpha = 4.5\, GM_{\text{BH}}/c^2$

in the BH shadow plots. However, we do not expect the results and conclusions to change substantially when these restrictions are lifted.

4.3 Semi-analytical results on the width of a black hole shadow

Some of the results presented in section 4.2 can be understood more easily if one makes a couple of (semi-) analytical observations. In particular, we will study the maximal horizontal width of the BH shadow boundary as a function of r_{max} and the total amount of DM in the halo.

For $r < r_{\text{min}}$, we know from the equations (3.27) and (3.30) that the metric function f is of the form

$$f(r) = C - \frac{2GM_{\text{BH}}}{c^2 r} \tag{4.1}$$

with $C = \exp\left\{-\frac{8\pi G}{c^2}\int_{r_{\text{min}}}^{r_{\text{max}}} r'\rho(r')\mathrm{d}r'\right\} \in (0,1]$ which, in particular, depends on r_{max} and the DM density profile. For simplicity, set $\theta_o = \pi/2$. The points where the BH shadow boundary in Bardeen's coordinates crosses the horizontal axis correspond to $\beta = 0$. With our choice of θ_o, this is equivalent to $\eta(r) = 0$ which can be shown to be equivalent to

$$R^3 - \frac{6}{C}R^2 + \frac{9}{C^2}R - \frac{4A^2}{C^2} = 0 \tag{4.2}$$

after using the explicit forms (3.45) and (4.1) of $\eta(r)$ and $f(r)$ and the shorthand notation $R := \frac{r}{GM_{\text{BH}}/c^2}$ and $A := \frac{a}{GM_{\text{BH}}/c^2}$. This cubic equation in R can be shown to have three distinct real solutions R_1, R_2 and R_3 of which only these two lie outside the (dimensionless) outermost event horizon (see section A.2 in the appendix for details):

$$R_1 = \frac{2}{C}\left[1 + \cos\left(\frac{2}{3}\arccos\left(|A|\sqrt{C}\right)\right)\right] \quad , \tag{4.3}$$

$$R_3 = \frac{2}{C}\left[1 + \cos\left(\frac{2}{3}\arccos\left(|A|\sqrt{C}\right) + \frac{4\pi}{3}\right)\right] < R_1 \tag{4.4}$$

This result is only valid as long as $R_1 < R_{\text{min}}$ because we used equation (4.1). For small $|A|$, this is satisfied because there $r_{\text{ms, massive, prograde}} \equiv r_{\text{min}}$ is rather large, as can be seen in figure 2.2. R_1 and R_3 provide the right and left crossing points of the BH shadow boundary of the α-axis. The horizontal 'diameter' d_α, i.e. the maximal size of the BH shadow in α-direction, is therefore

$$\begin{aligned} d_\alpha &= \alpha\left(R_1\frac{GM_{\text{BH}}}{c^2}\right) - \alpha\left(R_3\frac{GM_{\text{BH}}}{c^2}\right) \\ &= \left[\frac{CR_1^3 - 3R_1^2 + 2A^2R_1}{A(CR_1 - 1)} - \frac{CR_3^3 - 3R_3^2 + 2A^2R_3}{A(CR_3 - 1)}\right]\frac{GM_{\text{BH}}}{c^2} \end{aligned} \tag{4.5}$$

where we used equation (3.51). Note that R_1 and R_3 depend on C. For all A we can now plot d_α as a function of C for C slightly smaller than one as long as $R_1 < R_{\text{min}}$. The results are shown in figure 4.7.

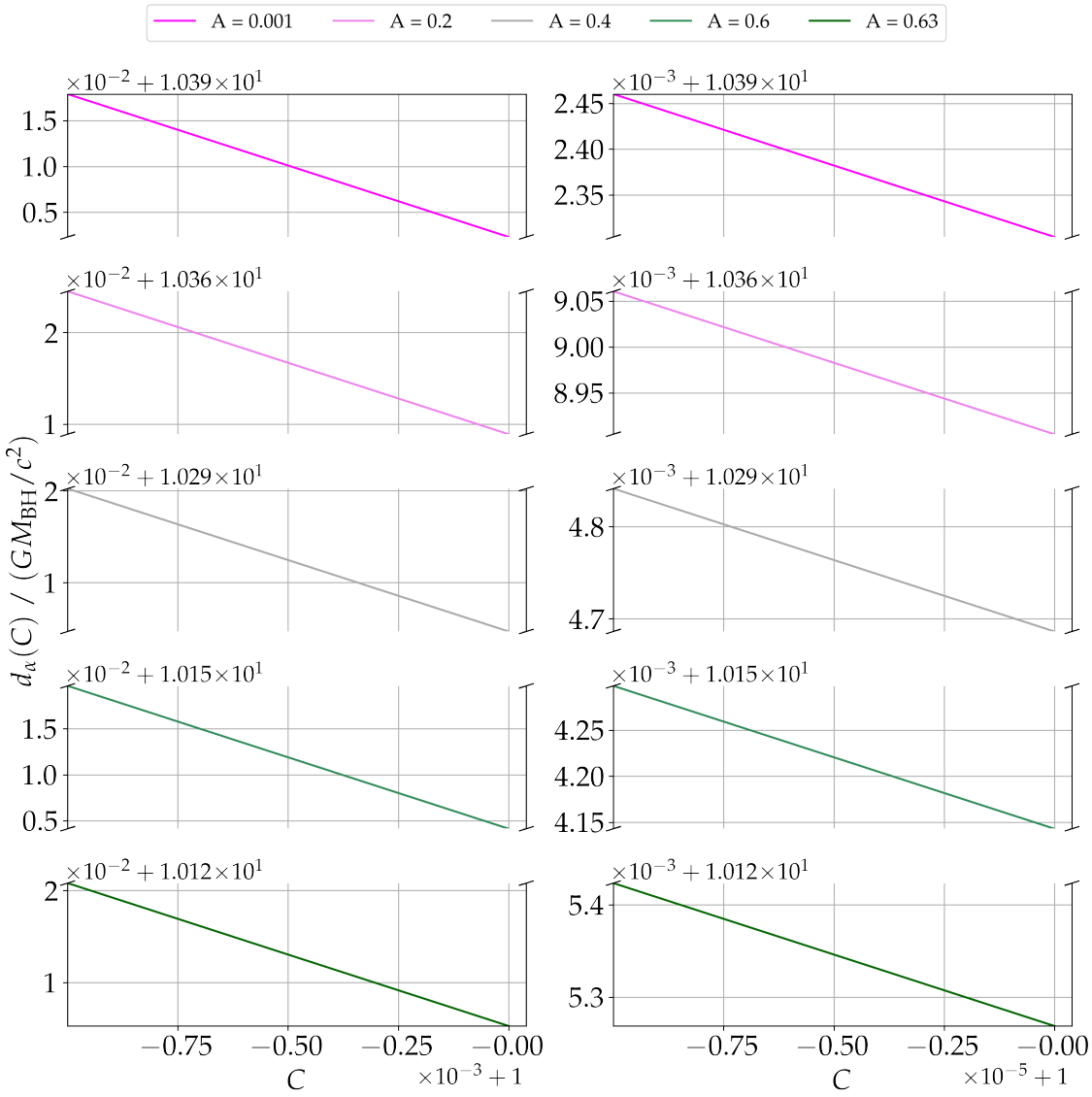

Figure 4.7: d_α as a function of C on two exemplary orders of magnitude for a couple of different spin parameters A. Larger A are not considered here because they violate $R_1 < R_{\text{min}}$.

One can see that $C \mapsto d_\alpha(C)$ can be approximated as affine linear in this region. Hence we can write $d_\alpha \approx -\lambda C + \mu$ for some $\lambda, \mu > 0$ that are independent of C and, as a consequence, also independent of r_{max} since C is the only place where r_{max} enters this analysis. Now define $\epsilon := \frac{8\pi G}{c^2} \int_{r_{\text{min}}}^{r_{\text{max}}} r' \rho(r') \mathrm{d}r'$. This quantity is a small positive number for all systems we are interested in. Since $C = \exp(-\epsilon)$, we can expand $C = 1 - \epsilon + \mathcal{O}(\epsilon^2)$ and obtain to first order in ϵ the connection

$$d_\alpha = (\mu - \lambda) + \lambda\epsilon \quad . \tag{4.6}$$

We can easily read off that for the vacuum case with $\epsilon = 0$ the BH shadow has a width of $\mu - \lambda$ and starting from this value d_α grows linearly in ϵ. Hence, within the model at hand and under the assumptions that have been made, the BH shadow width is directly related to $\int_{r_{\min}}^{r_{\max}} r'\rho(r')\mathrm{d}r'$ and not the total DM mass $4\pi \int_{r_{\min}}^{r_{\max}} r'^2\rho(r')\mathrm{d}r'$.

We can take this analysis a step further by noticing that all the density profiles in this thesis have the property that there is some radius r_{n} such that the density is an NFW profile outside of r_{n}. It follows that one can write $\epsilon = \delta + \frac{8\pi G}{c^2}\rho_0 r_0^2 \left(\frac{1}{1+r_{\mathrm{n}}/r_0} - \frac{1}{1+r_{\max}/r_0}\right)$ with δ being the contribution from between $r_{\min}$ and r_{n}. Therefore we have

$$d_\alpha = \mu - \lambda + \lambda\delta + \lambda\frac{8\pi G}{c^2}\rho_0 r_0^2 \left(\frac{1}{1+r_{\mathrm{n}}/r_0} - \frac{1}{1+r_{\max}/r_0}\right) \quad . \tag{4.7}$$

Now it is clear that d_α approaches a finite value for $r_{\max} \to \infty$. This means that for the systems in this thesis, the choice of $r_{\max}$ is not crucial for the absolute size of a BH shadow and for numerical purposes one should choose a very large value unless one has a good reason not to do so.

The situation is different when we consider a hypothetical density profile of the shape $\rho(r) = \rho_{\mathrm{p}}(r_{\mathrm{p}}/r)^\gamma$ in $[r_{\min}, r_{\max}]$, i.e. a pure power-law, and 0 otherwise. $r_{\mathrm{p}} \in \mathbb{R}^+$ is some constant radius, $\gamma \in \mathbb{R}^+$ and $\rho_{\mathrm{p}} = \rho(r_{\mathrm{p}})$. In this case we have

$$\epsilon = \begin{cases} \frac{8\pi G}{c^2}\rho_{\mathrm{p}} r_{\min}^2 (r_{\mathrm{p}}/r_{\min})^\gamma \frac{1-(r_{\min}/r_{\max})^{\gamma-2}}{\gamma-2} & \gamma \neq 2 \\ \frac{8\pi G}{c^2}\rho_{\mathrm{p}} r_{\mathrm{p}}^2 \ln(r_{\max}/r_{\min}) & \gamma = 2 \end{cases} \quad . \tag{4.8}$$

For $\gamma \leq 2$, ϵ diverges for $r_{\max} \to \infty$ which implies that one can achieve arbitrarily large d_α by simply choosing a large enough $r_{\max}$ (remember that λ and μ are independent of $r_{\max}$). In such a case it is important to make a very educated guess for a specific value of $r_{\max}$. In contrast, for $\gamma > 2$, ϵ converges to a finite value for $r_{\max} \to \infty$. Intuitively, this result means that the density has to decrease sufficiently fast in order for d_α to converge. As a cross-check, consider again an NFW profile. For large r, the density decreases approximately as r^{-3} which corresponds to a power law with $\gamma = 3 > 2$, implying that we should expect ϵ to converge for an NFW profile for $r_{\max} \to \infty$ and indeed it does as seen from equation (4.7).

4.4 Uncertainty and measurability estimates

Apart from the systematic errors and uncertainties that will be covered in section 4.5, there is also an uncertainty in the BH shadow sizes originating from the uncertainty of the parameters that entered the calculations. One parameter whose

effect on the BH shadows can be understood fairly easily is the NFW parameter ρ_0. We demonstrate the procedure on the example of a CDM halo around M87* with the properties $a = 0.5\,GM_{\mathrm{BH}}/c^2$, $r_{\mathrm{max}} = 10^{14}\,GM_{\mathrm{BH}}/c^2$. In order to be able to make use of the analysis from section 4.3, we also set $\theta_o = \pi/2$. According to [37], the NFW density parameter ρ_0 is expected to lie in the interval $(4\pi)^{-1}[10^{7.51-0.12}, 10^{7.51+0.13}]\,M_\odot\,\mathrm{kpc}^{-3} =: [\rho_{0,\,\mathrm{small}}, \rho_{0,\,\mathrm{large}}]$. To simplify the following, we assume $r_0 = 128.4\,\mathrm{kpc}$ [37] without any errors which is of course an enormous oversimplification since the uncertainty in r_0 is actually very large. From these pieces of information one can, for $\rho_{0,\,\mathrm{small}}$, ρ_0 as in table 3.1 and $\rho_{0,\,\mathrm{large}}$, calculate r_{min}, C, R_1 and R_3. The requirement $R_1 < R_{\mathrm{min}}$ turns out to be clearly fulfilled in all three cases, justifying the use of equations (4.3) and (4.4). Equation (4.5) finally yields $d_{\alpha,\,\mathrm{small}} \approx (10.235215 - 1.91 \cdot 10^{-4})\,GM_{\mathrm{BH}}/c^2$, $d_\alpha \approx 10.235215\,GM_{\mathrm{BH}}/c^2$ and $d_{\alpha,\,\mathrm{large}} \approx (10.235215 + 2.77 \cdot 10^{-4})\,GM_{\mathrm{BH}}/c^2$ for $\rho_{0,\,\mathrm{small}}$, ρ_0 and $\rho_{0,\,\mathrm{large}}$, respectively. Even though these values are fairly similar and might suggest that the error on ρ_0 is negligible, this is not quite true considering how alike all the BH shadows were. Looking at figure 4.8, one sees that the differences in the shown BH shadows' sizes are of the order of $10^{-5}\,GM_{\mathrm{BH}}/c^2$ or even smaller.
Taking into account the very ambitiously calculated errors for d_α from above, it becomes clear that the uncertainty in ρ_0 for the NFW profile alone could change the relative sizes of the BH shadows significantly. Of course one should mention that the parts of the BH shadows in figure 4.8 do not show d_α but they still give a good impression on the order of magnitude for the difference in d_α values. Furthermore, other uncertainties as for r_0 have not been taken into account at all, so it is reasonable to conclude that the uncertainties in parameters dominate over the small differences in BH shadow sizes and we expect this analysis to yield similar results for Sgr A* and different a, θ_o and r_{max}. The results for the spiked NFW profile stand out but a more careful analysis of the errors involved is necessary to estimate the reliability of these results.

The main purpose of the research in this thesis is to find out how tightly particle physical properties of DM could be constrained by observations of the geometry of BH shadows or if it is possible at all, see section 1.3. In order to answer this question, we want to understand how one could quantify the shadow geometry. We present the approach taken by [57] which captures the size and shape of a BH shadow by two quantities R_{s} and δ_{s} that are defined as follows: Let A be the point where the BH shadow boundary crosses the positive α-axis and set B and D to be the points where β is maximal and minimal, respectively. Then there exists a unique circle that passes through A, B and D and hence approximates the BH shadow boundary. R_{s} is defined to be the radius of this circle and is

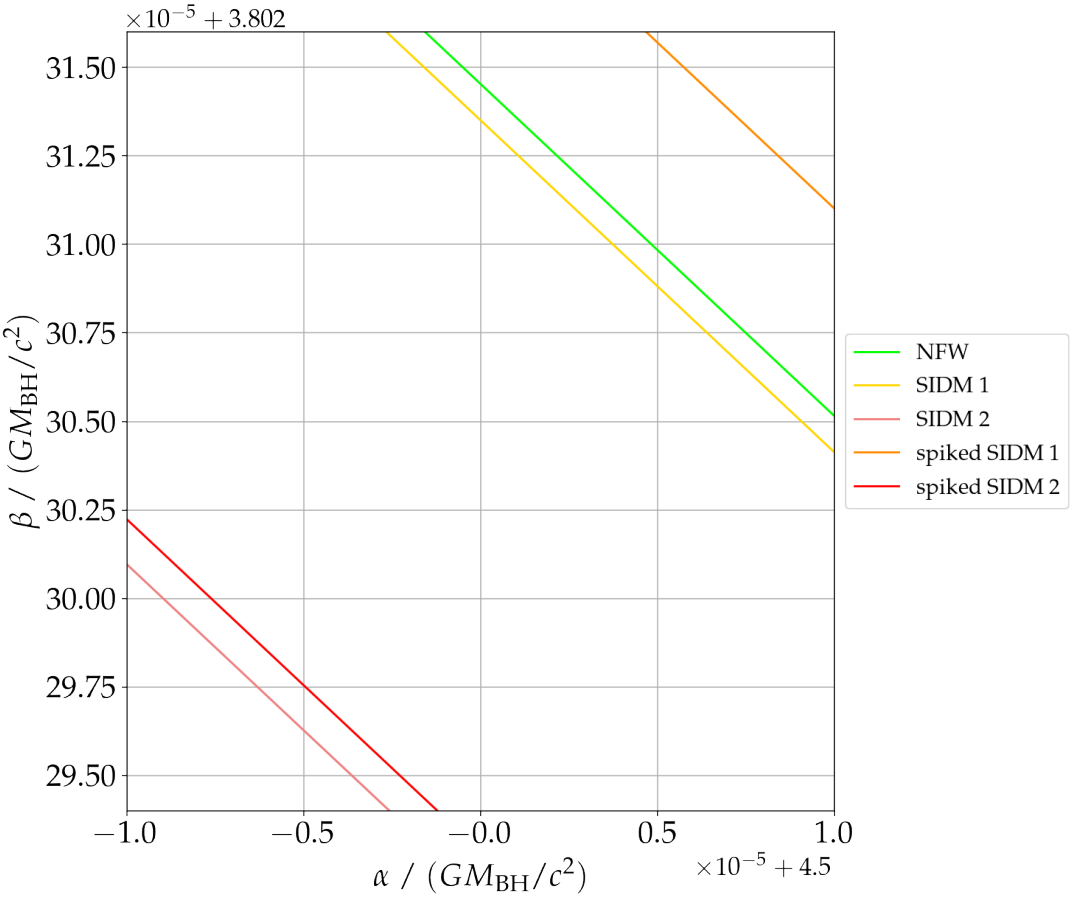

Figure 4.8: BH shadow boundaries of M87* with $a = 0.5\,GM_{\mathrm{BH}}/c^2$, $\theta_o = \pi/2$, $r_{\mathrm{max}} = 10^{14}\,GM_{\mathrm{BH}}/c^2$ around $\alpha = 4.5\,GM_{\mathrm{BH}}/c^2$. For ρ_0, the standard value of $(4\pi)^{-1} \cdot 10^{7.51}\,M_\odot\,\mathrm{kpc}^{-3}$ from [37] was used.

therefore a way to assign a radius to the in general non-circular shape of the BH shadow boundary. δ_s, on the other hand, measures how much the shape of the BH shadow boundary deviates from the fitting circle by relating the size of the 'dent' on the left side to R_s. If the distance between the left-most points of the BH shadow boundary and the fitting circle is denoted by d_s, then $\delta_s := d_s/R_s$. A sketch of the construction is shown in figure 4.9.

R_s may be used to find the angular diameter ϑ of the BH shadow for an observer on Earth. Letting $D_{\mathrm{BH}} \gg R_s$ be the distance between the Earth and the BH in question, we can write

$$\begin{aligned} \vartheta &= 2\arctan\left(\frac{R_s}{D_{\mathrm{BH}}}\right) \\ &\approx \frac{2R_s}{D_{\mathrm{BH}}} \\ &= b\frac{GM_{\mathrm{BH}}}{c^2 D_{\mathrm{BH}}} \\ &= b\vartheta_g \end{aligned} \tag{4.9}$$

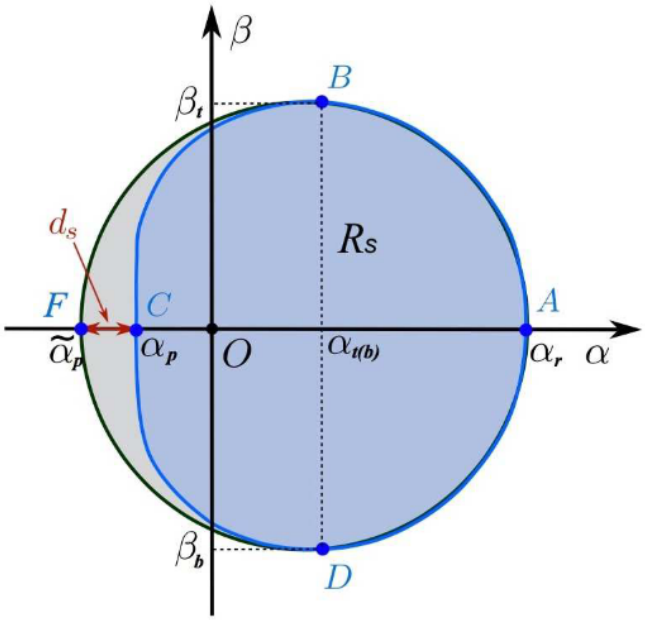

Figure 4.9: Illustration for the definition of R_s and δ_s. The figure is taken from [47].

for some dimensionless $b \in \mathbb{R}^+$. ϑ_g is called the angular gravitational radius. Using these observables, the authors in [47] arrive at the result that in order to even distinguish between the vacuum and a halo consisting of CDM around Sgr A*, one needs an angular resolution of $10^{-3}\,\mu$as which is far more precise than the 15 μas that are expected to be achievable in future EHT observations [58]. The Sgr A* shadows for the vacuum and a surrounding CDM halo are quite different in size relative to, say, the cases with SIDM 4 and spiked SIDM 4. As we saw in section 2.1.2, at least in the dwarf galaxy DDO 154 experimental evidence points towards cored density profiles as in our SIDM models. With this in mind, the chances of being able to tell apart two of the DM models in our discussion from the Sgr A* shadow geometry are slim. A halo described by a spiked NFW profile could be a bit more easily distinguished from the vacuum, but certainly not from the other DM models given the current resolution. The same conclusions should hold for M87* because the angular gravitational radius ϑ_g of M87* has been measured to be smaller than that of Sgr A* [20, 21]. Of course it is possible that the EHT or other (networks of) observatories will improve their resolutions even further in the near future, but an improvement by several orders of magnitude is probably out of reach.

In summary, it seems unlikely that anything new about the properties of DM can be learned from measurements of the Sgr A* and M87* shadow shapes and sizes alone in the next couple of years.

4.5 Limitations

The results presented here have certain limitations due to the simplicity of our models. Probably the biggest shortcoming of our approach is to completely neglect baryons and their interactions because the recent observations of Sgr A* and M87* show the BH shadows embedded in a luminous ring, see figure 1.2 again. Furthermore, our DM models were not very refined as they contained density spikes that were added by hand, velocity-independent self-interaction cross sections and they did not take quantum properties into account. On top of that, we also made the oversimplifying assumptions of a stationary and axisymmetric system. The construction of the metric (3.28) made use of a non-rigorous correspondence between Newtonian gravity and GR (recall the discussion below equation (3.15)) and the use of the Newman-Janis algorithm while keeping a spherically symmetric density profile in the equations raises the question what the density profile even means for $a \neq 0$. Finally, it is not clear at this point which energy-momentum tensor the spacetime geometry determined by (3.28) corresponds to and what the physical interpretation of that energy-momentum tensor could be.

5 Summary and outlook

In this thesis, we constructed density profiles for DM halos around Sgr A* and M87*, a spacetime metric for a rotating BH in a DM halo and visualized the resulting BH shadows of Sgr A* and M87* for an observer at infinity using Bardeen's coordinates. We also studied how the BH's spin parameter, the inclination angle of the observer and the halo's extent affect the shapes and the sizes of the BH shadows. In addition, we derived a concrete formula to estimate their widths given the DM density and made a very rough estimate of the uncertainty in this analysis stemming from the uncertainty of a density parameter.
What we found is that, within our framework and the limitations of the method, the BH's spin parameter and the observer's polar angle relative to the axis of symmetry have the strongest effects on the BH shadows. The larger the spin parameter, the stronger the deformation and horizontal shift of the BH shadows in the α-β plane, and these transformations are the most effective when the observer is located in the equatorial plane. In addition to that, we saw that, for a fixed BH, spin parameter and observer position, the various DM models do not lead to significantly different BH shadows. Relative deviations are on the order of $\lesssim 10^{-3}\, GM_{\mathrm{BH}}/c^2$, measured in Bardeen coordinates. Among all DM models, the spiked NFW model always results in the largest BH shadows while the spike-less SIDM model with the largest self-interaction cross section leads to the smallest. Systems with density spikes always exhibit larger BH shadows than their respective counterparts without spikes, the BH shadows grow when the cross section for SIDM decreases and these observations can be easily explained by the shape of the DM density profiles. DM densities at large distances from the BH, albeit small, cannot be neglected as they might change the relative sizes of the BH shadows. Therefore, one needs a good reason to pick a specific value for r_{max} in a concrete system.
All of these aspects are true both for Sgr A* and M87*. One clear difference between these two systems is that the spike and matching radii are further away from Sgr A* than from M87*, causing the density spikes to have a stronger impact on the shadows of Sgr A* at intermediate halo radii r_{max}. It also makes the relative BH shadow sizes stabilize at larger halo sizes in the Sgr A* system. This stable ordering in size is almost identical between both BHs. The only difference is the NFW and the spiked SIDM 1 models switching positions which can be understood by a look at their densities.
In general, all the DM effects on the BH shadows of Sgr A* and M87* are tiny. As explained in section 4.4, it seems highly unlikely that it will be possible for any observatory or network of individual observatories to reach a sufficiently high angular resolution within the next couple of years.

Of course these conclusions only hold within our framework which has its weaknesses. One way to avoid at least some of the problems from section 4.5 in future research could be to derive an energy-momentum tensor from given accretion disk and DM halo models for the right-hand side of the Einstein equations. Although it would surely demand advanced numerical methods, the Einstein equations could be solved and hence provide a solid general relativistic description of the system. Of course finding adequate models for the accretion disk and the DM halo is quite challenging and certainly also needs a lot more work.

Despite its limitations, our result that possible DM effects on the BH shadows of Sgr A* and M87* are too small to be observable as of now may still be a hint that it is important to continue the ongoing work on improving the resolution of observatories. In addition to that, it is also useful to conduct studies on other observables of BH systems that might allow conclusions about DM properties. Furthermore, as explained in section 1.1, there is a number of physical systems that point to the existence of DM and that can still serve as laboratories for its properties. In parallel, the alternative approach of trying to solve the missing mass problem by modified gravity theories might also be helpful in illuminating the nature of DM.

References

[1] *Rotation curve*. https://astronomy.swin.edu.au/cosmos/r/rotation+curve. Accessed: November 21, 2022.

[2] M. S. Roberts. "The Rotation Curve of Galaxies." In: *Dynamics of the Solar Systems*. Ed. by Avram Hayli. Vol. 69. Jan. 1975, p. 331.

[3] Bryn Jones and Prasenjit Saha. *THE GALAXY*. https://www.astro.umd.edu/~richard/ASTRO620/QM_chap5.pdf. Accessed: November 21, 2022.

[4] V. C. Rubin, Jr. Ford W. K., and N. Thonnard. "Rotational properties of 21 SC galaxies with a large range of luminosities and radii, from NGC 4605 (R=4kpc) to UGC 2885 (R=122kpc)." In: *The Astrophysical Journal* 238 (June 1980), pp. 471–487. DOI: 10.1086/158003.

[5] Adriana Araujo, Diego López Restrepo, and Jose Pereira. "De Sitter-Invariant Special Relativity and Galaxy Rotation Curves." In: *Gravitation and Cosmology* 25 (June 2017). DOI: 10.1134/S0202289319020026.

[6] F. Zwicky. "Die Rotverschiebung von extragalaktischen Nebeln." In: *Helvetica Physica Acta* 6 (Jan. 1933), pp. 110–127.

[7] Thomas Lacroix. "Phenomenology of dark matter particles at the centers of galaxies." Theses. Université Pierre et Marie Curie - Paris VI, July 2016. URL: https://tel.archives-ouvertes.fr/tel-01369006.

[8] CERN. *Dark Matter*. https://home.cern/science/physics/dark-matter. Accessed: November 27, 2022.

[9] Gianfranco Bertone and Tim M. P. Tait. "A new era in the search for dark matter." In: *Nature* 562.7725 (Oct. 2018), pp. 51–56. DOI: 10.1038/s41586-018-0542-z. URL: https://doi.org/10.1038%2Fs41586-018-0542-z.

[10] K. Schwarzschild. "On the Gravitational Field of a Mass Point According to Einstein's Theory." In: *Abh. Konigl. Preuss. Akad. Wissenschaften Jahre 1906,92, Berlin,1907* 1916 (Jan. 1916), pp. 189–196.

[11] Pankaj Sharan. *Spacetime, Geometry and Gravitation*. Birkhäuser Basel, 2009. DOI: 10.1007/978-3-7643-9971-9.

[12] B. Goutéraux. *Black-Hole Solutions to Einstein's Equations in the Presence of Matter and Modifications of Gravitation in Extra Dimensions*. 2010. DOI: 10.48550/ARXIV.1011.4941. URL: https://arxiv.org/abs/1011.4941.

[13] Jeremy Schnittman. "A brief history of black holes." In: *Astronomy* (Oct. 2016). Accessed: November 26, 2022. URL: https://astronomy.com/magazine/2019/08/a-brief-history-of-black-holes.

[14] J. R. Oppenheimer and H. Snyder. "On Continued Gravitational Contraction." In: *Phys. Rev.* 56 (5 Sept. 1939), pp. 455–459. DOI: 10.1103/PhysRev.56.455. URL: https://link.aps.org/doi/10.1103/PhysRev.56.455.

[15] C. T. Bolton. "Identification of Cygnus X-1 with HDE 226868." In: *Nature* 235.5336 (Feb. 1972), pp. 271–273. DOI: 10.1038/235271b0.

[16] Cosimo Bambi. "Astrophysical Black Holes: A Review." In: *Proceedings of Multifrequency Behaviour of High Energy Cosmic Sources - XIII — PoS(MULTIF2019)*. Sissa Medialab, Nov. 2020. DOI: 10.22323/1.362.0028. URL: https://doi.org/10.22323%2F1.362.0028.

[17] V. I. Dokuchaev, Yu. N. Eroshenko, and S. G. Rubin. *Origin of supermassive black holes*. 2007. DOI: 10.48550/ARXIV.0709.0070. URL: https://arxiv.org/abs/0709.0070.

[18] John Kormendy and Douglas Richstone. "Inward Bound—The Search For Supermassive Black Holes In Galactic Nuclei." In: *Annual Review of Astronomy and Astrophysics* 33 (Jan. 1995), p. 581. DOI: 10.1146/annurev.aa.33.090195.003053.

[19] NASA/IPAC Extragalactic Database. *REDSHIFT-INDEPENDENT DISTANCES for MESSIER 087*. http://ned.ipac.caltech.edu/cgi-bin/objsearch?objname=NGC+4486&extend=no&hconst=73&omegam=0.27&omegav=0.73&corr_z=1&out_csys=Equatorial&out_equinox=J2000.0&obj_sort=RA+or+Longitude&of=pre_text&zv_breaker=30000.0&list_limit=5&img_stamp=YES. Accessed: November 18, 2022.

[20] The Event Horizon Telescope Collaboration. "First Sagittarius A* Event Horizon Telescope Results. I. The Shadow of the Supermassive Black Hole in the Center of the Milky Way." In: *The Astrophysical Journal Letters* 930.L12 (2022). URL: https://doi.org/10.3847/2041-8213/ac6674.

[21] The Event Horizon Telescope Collaboration. "First M87 Event Horizon Telescope Results. I. The Shadow of the Supermassive Black Hole." In: (2019). eprint: Arxiv:1906.11238v1. URL: https://arxiv.org/abs/1906.11238.

[22] Event Horizon Telescope Collaboration. *Understanding Accretion Around A Black Hole*. https://eventhorizontelescope.org/science/. Accessed: November 26, 2022.

[23] Volker Perlick and Oleg Yu. Tsupko. "Calculating black hole shadows: Review of analytical studies." In: *Physics Reports* 947 (Feb. 2022), pp. 1–39. DOI: 10.1016/j.physrep.2021.10.004. URL: https://doi.org/10.1016%2Fj.physrep.2021.10.004.

[24] *Black Hole Shadow*. https://odysseyedu.wordpress.com/black-hole-shadow/. Accessed: November 25, 2022.

[25] Risa H. Wechsler and Jeremy L. Tinker. "The Connection Between Galaxies and Their Dark Matter Halos." In: *Annual Review of Astronomy and Astrophysics* 56.1 (Sept. 2018), pp. 435–487. DOI: 10.1146/annurev-astro-081817-051756. URL: https://doi.org/10.1146%2Fannurev-astro-081817-051756.

[26] Julio F. Navarro, Carlos S. Frenk, and Simon D. M. White. "A Universal Density Profile from Hierarchical Clustering." In: *The Astrophysical Journal* 490.2 (Dec. 1997), pp. 493–508. DOI: 10.1086/304888. URL: https://doi.org/10.1086%2F304888.

[27] Sean Tulin and Hai-Bo Yu. "Dark matter self-interactions and small scale structure." In: *Physics Reports* 730 (Feb. 2018), pp. 1–57. DOI: 10.1016/j.physrep.2017.11.004. URL: https://doi.org/10.1016%2Fj.physrep.2017.11.004.

[28] Manoj Kaplinghat, Sean Tulin, and Hai-Bo Yu. "Dark Matter Halos as Particle Colliders: Unified Solution to Small-Scale Structure Puzzles from Dwarfs to Clusters." In: *Phys. Rev. Lett.* 116 (4 Jan. 2016), p. 041302. DOI: 10.1103/PhysRevLett.116.041302. URL: https://link.aps.org/doi/10.1103/PhysRevLett.116.041302.

[29] Romeel Dave et al. "Halo Properties in Cosmological Simulations of Self-interacting Cold Dark Matter." In: *The Astrophysical Journal* 547.2 (Feb. 2001), pp. 574–589. DOI: 10.1086/318417. URL: https://doi.org/10.1086%2F318417.

[30] Paolo Gondolo and Joseph Silk. "Dark Matter Annihilation at the Galactic Center." In: *Physical Review Letters* 83.9 (Aug. 1999), pp. 1719–1722. DOI: 10.1103/physrevlett.83.1719. URL: https://doi.org/10.1103%2Fphysrevlett.83.1719.

[31] Robert M. Wald. *General relativity*. Chicago, IL: Chicago Univ. Press, 1984.

[32] Sebastian Boblest, Thomas Müller, and Günter Wunner. *Spezielle und allgemeine Relativitätstheorie*. Heidelberger Platz 3, 14197 Berlin, Germany: Springer Spektrum Berlin, Heidelberg, 2022. DOI: 10.1007/978-3-662-63352-6.

[33] James M. Bardeen, William H. Press, and Saul A. Teukolsky. "Rotating Black Holes: Locally Nonrotating Frames, Energy Extraction, and Scalar Synchrotron Radiation." In: *The Astrophysical Journal* 178 (Dec. 1972), pp. 347–370. DOI: 10.1086/151796.

[34] Edward Teo. "Spherical orbits around a Kerr black hole." In: *General Relativity and Gravitation* 53.1 (Jan. 2021). DOI: 10.1007/s10714-020-02782-z. URL: https://doi.org/10.1007%2Fs10714-020-02782-z.

[35] Edward Teo. *Existence and Properties of the Spherical Photon Orbits*. https://phyweb.physics.nus.edu.sg/~phyteoe/kerr/. Accessed: November 25, 2022.

[36] P. L. C. de Oliveira, J. A. de Freitas Pacheco, and G. Reinisch. "Testing two alternative theories to dark matter with the Milky Way dynamics." In: *General Relativity and Gravitation* 47.2 (Jan. 2015). DOI: 10.1007/s10714-014-1849-1. URL: https://doi.org/10.1007%2Fs10714-014-1849-1.

[37] L. Oldham and M. Auger. "Galaxy structure from multiple tracers: II. M87 from parsec to megaparsec scales." In: *Monthly Notices of the Royal Astronomical Society* 457 (Jan. 2016). DOI: 10.1093/mnras/stv2982.

[38] Lukas Hölker. "Gravitational Wave Probes of Self-Interacting Dark Matter." (unpublished). Sept. 2021.

[39] Lukas Hölker. 2021. URL: https://github.com/Lukas-Hoelker/SIDM-GWs/blob/main/Lukas_Halos_natunits_mod3.ipynb.

[40] Gerardo Alvarez and Hai-Bo Yu. "Density spikes near black holes in self-interacting dark matter halos and indirect detection constraints." In: *Physical Review D* 104.4 (Aug. 2021). DOI: 10.1103/physrevd.104.043013. URL: https://doi.org/10.1103%2Fphysrevd.104.043013.

[41] David Merritt. *Single and Binary Black Holes and their Influence on Nuclear Structure*. 2003. DOI: 10.48550/ARXIV.ASTRO-PH/0301257. URL: https://arxiv.org/abs/astro-ph/0301257.

[42] David Merritt. "Evolution of the Dark Matter Distribution at the Galactic Center." In: *Physical Review Letters* 92.20 (May 2004). DOI: 10.1103/physrevlett.92.201304. URL: https://doi.org/10.1103%2Fphysrevlett.92.201304.

[43] S. Gillessen et al. "MONITORING STELLAR ORBITS AROUND THE MASSIVE BLACK HOLE IN THE GALACTIC CENTER." In: *The Astrophysical Journal* 692.2 (Feb. 2009), pp. 1075–1109. DOI: 10.1088/0004-637x/692/2/1075. URL: https://doi.org/10.1088%2F0004-637x%2F692%2F2%2F1075.

[44] Kazunori Akiyama et al. "First M87 Event Horizon Telescope Results. VI. The Shadow and Mass of the Central Black Hole." In: *Astrophys. J. Lett.* 875.1 (2019), p. L6. DOI: 10.3847/2041-8213/ab1141. arXiv: 1906.11243 [astro-ph.GA].

[45] Tonatiuh Matos and Dario Nunez. "The general relativistic geometry of the Navarro-Frenk-White model." In: (2003). DOI: 10.48550/ARXIV.ASTRO-PH/0303594. URL: https://arxiv.org/abs/astro-ph/0303594.

[46] Zhaoyi Xu et al. "Black hole space-time in dark matter halo." In: *Journal of Cosmology and Astroparticle Physics* 2018.09 (Sept. 2018), pp. 038–038. DOI: 10.1088/1475-7516/2018/09/038. URL: https://doi.org/10.1088%2F1475-7516%2F2018%2F09%2F038.

[47] Xian Hou et al. "Black hole shadow of Sgr A* in dark matter halo." In: *Journal of Cosmology and Astroparticle Physics* 2018.07 (July 2018), pp. 015–015. ISSN: 1475-7516. DOI: 10.1088/1475-7516/2018/07/015. URL: http://dx.doi.org/10.1088/1475-7516/2018/07/015.

[48] Isaac Chavel. "Riemannian Manifolds." In: *Riemannian Geometry: A Modern Introduction*. 2nd ed. Cambridge Studies in Advanced Mathematics. Cambridge University Press, 2006, pp. 1–55. DOI: 10.1017/CBO9780511616822.003.

[49] E. T. Newman and A. I. Janis. "Note on the Kerr Spinning-Particle Metric." In: *Journal of Mathematical Physics* 6.6 (1965), pp. 915–917. DOI: 10.1063/1.1704350. eprint: https://doi.org/10.1063/1.1704350. URL: https://doi.org/10.1063/1.1704350.

[50] Harold Erbin. "Janis–Newman Algorithm: Generating Rotating and NUT Charged Black Holes." In: *Universe* 3.1 (Mar. 2017), p. 19. DOI: 10.3390/universe3010019. URL: https://doi.org/10.3390%2Funiverse3010019.

[51] Brandon Carter. "Global Structure of the Kerr Family of Gravitational Fields." In: *Phys. Rev.* 174 (5 Oct. 1968), pp. 1559–1571. DOI: 10.1103/PhysRev.174.1559. URL: https://link.aps.org/doi/10.1103/PhysRev.174.1559.

[52] Sébastien C. Garmier. *The Shadow of a Rotating Black Hole*. May 2021. URL: https://www.physik.uzh.ch/dam/jcr:b574157a-3609-4a69-aded-e5e5ebcdbbe5/Semesterarbeit_S%C3%A9bastien_Garmier.pdf.

[53] J. M. Bardeen. "Timelike and null geodesics in the Kerr metric." In: *Les Houches Summer School of Theoretical Physics: Black Holes*. 1973, pp. 215–240.

[54] S.E. Vázquez and E.P. Esteban. "Strong-field gravitational lensing by a Kerr black hole." In: *Il Nuovo Cimento B* 119.5 (Dec. 2004), pp. 489–519. ISSN: 03693554, 03693554. DOI: 10.1393/ncb/i2004-10121-y. URL: https://doi.org/10.1393/ncb/i2004-10121-y.

[55] Lukas Prinz et al. 2022. URL: https://github.com/prinzlukas/BH-shadows-and-Dark-Matter/tree/main/BHshadow_calculation_Nov22.

[56] J. Richard Gott III et al. "A Map of the Universe." In: *The Astrophysical Journal* 624.2 (May 2005), pp. 463–484. DOI: 10.1086/428890. URL: https://doi.org/10.1086%2F428890.

[57] Kenta Hioki and Kei-ichi Maeda. "Measurement of the Kerr spin parameter by observation of a compact object's shadow." In: *Physical Review D* 80.2 (July 2009). DOI: 10.1103/physrevd.80.024042. URL: https://doi.org/10.1103%2Fphysrevd.80.024042.

[58] Event Horizon Telescope Collaboration. *Improving the Resolution of the EHT*. Accessed: November 18, 2022. URL: https://eventhorizontelescope.org/technology.

[59] Eric W. Weisstein. *Cubic Formula*. Accessed: November 3, 2022. URL: https://mathworld.wolfram.com/CubicFormula.html.

A Appendix

A.1 Existence of an outermost event horizon

For $r < r_{\min}$, the condition $\Delta(r) = 0$ for an event horizon has the shape

$$r^2\left(C - \frac{2GM_{\mathrm{BH}}}{c^2 r}\right) + a^2 = 0 \quad \Leftrightarrow \quad r^2 - \frac{2GM_{\mathrm{BH}}}{c^2 C} r + \frac{a^2}{C} = 0 \tag{A.1}$$

with $C = \exp\left\{-\frac{8\pi G}{c^2}\int_{r_{\min}}^{r_{\max}} r'\rho(r')\mathrm{d}r'\right\} \in (0,1]$. This quadratic equation is solved by

$$r_{1,2} = \frac{1}{C}\left[\frac{GM_{\mathrm{BH}}}{c^2} \pm \sqrt{\left(\frac{GM_{\mathrm{BH}}}{c^2}\right)^2 - a^2 C}\right] \quad . \tag{A.2}$$

For $|a| \in (0,1)\, GM_{\mathrm{BH}}/c^2$, these are indeed two distinct real and positive solutions because

$$\begin{aligned} 0 &= \left(\frac{GM_{\mathrm{BH}}}{c^2}\right)^2 - \left(\frac{GM_{\mathrm{BH}}}{c^2}\right)^2 \\ &\leq \left(\frac{GM_{\mathrm{BH}}}{c^2}\right)^2 - \left(\frac{GM_{\mathrm{BH}}}{c^2}\right)^2 C \\ &< \left(\frac{GM_{\mathrm{BH}}}{c^2}\right)^2 - a^2 C \\ &< \left(\frac{GM_{\mathrm{BH}}}{c^2}\right)^2 \quad . \end{aligned} \tag{A.3}$$

In addition, the smaller solution r_2 is smaller than $\frac{1}{C}\frac{GM_{\mathrm{BH}}}{c^2}$ which, for our purposes where C is only very slightly below 1, is smaller than $r_{\min}$ for all spin parameters that we are interested in. This means that at least r_2 is a valid solution to $\Delta(r) = 0$. There could be more and larger solutions, but this is not a problem: If there are finitely many solutions, we simply take r_{oeh} to be the largest of those. In the unlikely case that there are infinitely many, we could set r_{oeh} to be the supremum of the set of roots which is guaranteed to exist: Since f has a unique root r_* and f is strictly increasing, we have $\Delta(r) = r^2 f(r) + a^2 > a^2 > 0$ for $r > r_*$, so the set of roots is bounded from above and non-empty.

A.2 Solutions to equation (4.2)

If we use the definition in [59], it is clear that the discriminant D of equation (4.2) is $D = \frac{4A^2}{C^5}(A^2C - 1)$ which is negative for $0 < A^2 < 1/C$. This is always the case in what we want to consider because $0 < |A| < 1$ and $C \leq 1$. It follows

that there are three distinct real solutions R_1, R_2 and R_3 to (4.2) which are given by

$$R_k = \frac{2}{C}\left[1+\cos\left(\frac{\arccos(2A^2C-1)+2\pi(k-1)}{3}\right)\right] \quad , \quad k=1,2,3 \quad . \tag{A.4}$$

With the identity $\arccos(2x^2-1) = 2\arccos(x)$ for $x \in \mathbb{R}_0^+$ which can be derived from the double-angle formula for cos, this can be turned into

$$R_k = \frac{2}{C}\left[1+\cos\left(\frac{2}{3}\arccos(|A|\sqrt{C})+(k-1)\frac{2\pi}{3}\right)\right] \quad , \quad k=1,2,3 \quad . \tag{A.5}$$

We want to see which of these solutions are positive and lie outside the outermost event horizon R_{oeh} which, as we see from section A.1, is given by

$$R_{\text{oeh}} = \frac{1}{C}\left(1+\sqrt{1-A^2C}\right) \quad . \tag{A.6}$$

In order to do this, notice that $\frac{2}{3}\arccos(|A|\sqrt{C}) \in (0,\pi/3)$ and, as a consequence, $R_1 \in (3,4)\,\frac{1}{C}$, $R_2 \in (0,1)\,\frac{1}{C}$ and $R_3 \in (1,3)\,\frac{1}{C}$. For the outermost event horizon, we obviously have $R_{\text{oeh}} \in (1,2)\,\frac{1}{C}$. From these observations it already follows that $R_1 > R_3 > R_2$ and $R_1 > R_{\text{oeh}} > R_2$. The relative position of R_3 and R_{oeh}, however, is not clear at this point but it can be obtained by noticing that with $\psi := \frac{2}{3}\arccos\left(|A|\sqrt{C}\right)+\frac{4\pi}{3} \in (4\pi/3, 5\pi/3)$, we have

$$\begin{aligned}
& R_3 > R_{\text{oeh}} \\
\Leftrightarrow \quad & (1+2\cos(\psi))^2 > 1-\cos^2\left(\tfrac{3}{2}\psi\right) \\
\Leftrightarrow \quad & 4\cos^2(\psi)+4\cos(\psi) > -\left(2\cos^3(\psi)-\tfrac{3}{2}\cos(\psi)+\tfrac{1}{2}\right) \\
\Leftrightarrow \quad & 2\left(\cos(\psi)+1\right)\left(\cos(\psi)+\tfrac{1}{2}\right)^2 > 0
\end{aligned} \tag{A.7}$$

which is true because $\cos(\psi) \in (-1/2, 1/2)$. In summary, we have $R_1 > R_3 > R_{\text{oeh}} > R_2 > 0$.

B Acknowledgments

First and foremost, I want to thank Prof. Laura Sagunski for giving me the opportunity to work in such an interesting field of research, for providing a comfortable working atmosphere in the entire working group as well as during the individual meetings, for guiding me through this project and for being accessible for questions at all times. I also want to thank Dr. Alejandro Cruz-Osorio for taking his time to discuss the topic with me and for answering questions. I also enjoyed working together with Niklas Becker, Dr. Saeed Rastgoo and Jorden Roberts who made very useful comments on my project and were always happy to help. In particular, I thank Niklas Becker for helping me a lot with programming in Python and for speeding up parts of my code, Dr. Saeed Rastgoo for sharing Mathematica codes with me and Jorden Roberts for spending a lot of time on doing the r_{min} calculations and writing a root-finding algorithm that is used in many parts of the BH shadow code. Furthermore, I am very grateful to Lukas Hölker for writing and letting me use a big part of the code calculating the DM density profiles. I will also take the opportunity to thank Dr. Frederic Schuller for publicly sharing his outstanding lectures that have given me many invaluable insights in Mathematics and Physics throughout the past years. Of I course I also want to express my gratitude to those who proofread this thesis and made important remarks. Last but not least, I wish to thank my family, my partner and my friends for being so supportive at any time.

C Declaration of originality

Hiermit erkläre ich, dass ich die Arbeit selbstständig und ohne Benutzung anderer als der angegebenen Quellen und Hilfsmittel verfasst habe. Alle Stellen der Arbeit, die wörtlich oder sinngemäß aus Veröffentlichungen oder aus anderen fremden Texten entnommen wurden, sind von mir als solche kenntlich gemacht worden. Ferner erkläre ich, dass die Arbeit nicht - auch nicht auszugsweise - für eine andere Prüfung verwendet wurde.

Frankfurt am Main, den 29. November 2022

Lukas Prinz